Modeling the Wound healing in Necrotizing Enterocolitis and Diabetic Foot Ulcer

by

Qi Mi

B.S., Nanjing University, China, 2002

M.A., University of Pittsburgh, 2004

Submitted to the Graduate Faculty of

Arts and Science in partial fulfillment

of the requirements for the degree of

Doctor of Philosophy

University of Pittsburgh

2007

UNIVERSITY OF PITTSBURGH

ARTS AND SCIENCE

This dissertation was presented

by

Qi Mi

It was defended on

August 30, 2007

and approved by

Béatrice Rivière, PhD, Associate Professor, Department of Mathematics

David Swigon, PhD, Assistant Professor, Department of Mathematics

Bard Ermentrout, PhD, Professor, Department of Mathematics

Ivan Yotov, PhD, Professor, Department of Mathematics

David Hackam, MD, PhD, Assistant Professor, Department of Surgery

Yoram Vodovotz, PhD, Associate Professor, Department of Surgery

Dissertation Advisor: Béatrice Rivière, David Swigon, Department of Mathematics

MODELING THE WOUND HEALING IN NECROTIZING ENTEROCOLITIS AND DIABETIC FOOT ULCER

Qi Mi, PhD

University of Pittsburgh, 2007

In my thesis, I present three different models for the wound healing in Necrotizing Enterocolitis and Diabetic Foot Ulcer. (I) NEC results after an injury to the mucosal lining of the intestine, leading to translocation of bacteria and endotoxin. Intestinal mucosal defects are repaired by the process of intestinal restitution, during which enterocytes migrate from healthy areas to sites of injury. To model the migration of enterocytes, first we formulate a one-dimensional mathematical model based on the assumption of elastic deformation of the cell layer. Then we extend the model into a two-dimension space and the resulting moving boundary problem is solved by using modified Finite Element Method. (II) Diabetic foot ulcers (DFU) are caused by both vascular and neurologic complications of diabetes, in combination with persistent opportunistic infections and deficient wound healing. We develop an Agent-based computational model to simulate its inflammation and the resolution of the inflammatory response in its wound healing process.

TABLE OF CONTENTS

LIST OF TABLES

LIST OF FIGURES

PREFACE

This is my three years of research work in the field of applied mathematics in biology. During this period, I feel extremely lucky and honored to be mentored by a group of excellent researchers at University of Pittsburgh. First and foremost, I would like to thank my advisors: Dr. Riviere and Dr. Swigon. Their support and guidance have been invaluable to me throughout my doctoral research. I would also like to thank Dr. Yotov who initially brought me into this field and Dr. Ermentrout for his knowledge and enthusiasm that inspired me in my research. I am also grateful to Dr. Hackam for his great input of biology and Dr. Cetin for providing the cell migration data.

I would like to give special thanks to Dr. Vodovotz. Without his great effort, I would never have chance to have such good projects. Thanks for his tremendous interest and support in my research.

Finally I would like to thank my parents for supporting me in educational pursuits.

1.0 INTRODUCTION

1.1 NECROTIZING ENTEROCOLITIS

Necrotizing enterocolitis (NEC) is the leading cause of death from gastrointestinal disease in preterm infants. "Necrotizing" means damage and death of cells; "entero" refers to the intestine; "colitis" means inflammation of the colon (lower part of the intestine). With mortality rates approaching 50% in infants who weigh less than 1500 g, NEC represents a significant clinical problem. Although, it is more common in premature infants, it can also be observed in term babies. It results from an injury to the mucosal lining of the intestine, leading to translocation of bacteria and endotoxin into the circulation. Intestinal mucosal defects are repaired by the process of intestinal restitution, during which enterocytes migrate from healthy areas to sites of injury.

In my thesis, first we develop a mathematical model of migration of enterocytes during experimental NEC in one-dimensional space (35). The model is based on a novel assumption of elastic deformation of the cell layer and incorporates the following effects (i) mobility promoting force due to lamellipod formation, (ii) mobility impeding adhesion to the cell matrix, and (iii) enterocyte proliferation. Our model successfully reproduces the behavior observed for enterocyte migration on glass coverslips, namely the dependence of migration speed on the distance from the wound edge, and the finite propagation distance in the absence of proliferation which results

in an occasional failure to close the wound. It also qualitatively reproduces the dependence of migration speed on integrin concentration. The model is applicable to the closure of a wound with a linear edge and, after calibration with experimental data, could be used to predict the effect of chemical agents on mobility, adhesion, and proliferation of enterocytes. Secondly to model a more general scenario, we derive a two-dimensional partial-differential model based on the laws of continuum mechanics and it is analogous to Darcy's law in the theory of flow through porous media. The resulting moving-boundary problem is numerically solved by using modified finite element method. Although for the current model, we only consider the case for the absence of proliferation, like our 1d model, it also successfully reproduces the behavior observed for enterocytes migration.

1.2 DIABETIC FOOT ULCER

Inflammation and wound healing are inextricably linked and complex processes, and are deranged in the setting of chronic, non-healing diabetic foot ulcers (DFU). An ideal therapy for DFU should both suppress excessive inflammation while enhancing healing. We reasoned that biological simulation would clarify mechanisms and help refine therapeutic approaches to DFU. We developed an agent-based model (ABM) capable of reproducing qualitatively much of the literature data on skin wound healing, including changes in relevant cell populations (macrophages, neutrophils, fibroblasts) and their key effector cytokines (tumor necrosis factor-α

[TNF], interleukin [IL]-1β, IL-10, and transforming growth factor-β1 [TGF-β1]) (62). In this simulation, a normal healing response results in tissue damage that first increases (due to wound-induced inflammation) and then decreases as collagen levels increase. Studies by others suggest that diabetes and DFU are characterized by elevated TNF and reduced TGF-β1, though which of these changes is a cause and which one is an effect is unclear. Accordingly, we simulated the genesis of DFU in two ways, either by 1) increasing the rate of TNF production fourfold, or 2) by decreasing the rate of TGF-β1 production 67% based on prior literature. Both manipulations resulted in increased inflammation (elevated neutrophils, TNF, and tissue damage), and delayed healing (reduced TGF-β1 and collagen). Our ABM reproduced the therapeutic effect of PDGF/ platelet releasate treatment as well as DFU debridement. We next simulated the expected effect of administering 1) a neutralizing anti-TNF antibody, 2) an agent that would increase the activation of endogenous latent TGF-β1, or 3) latent TGF-β1 (which has a longer half-life than active TGF-β1), and found that these therapies would have similar effects regardless of the initial assumption of the derangement that underlies DFU (elevated TNF vs. reduced TGF-β1).

2.0 ONE-DIMENSIONAL ELASTIC CONTINUUM MODEL OF ENTEROCYTE LAYER MIGRATION

In this chapter, I describe our one-dimensional elastic continuum model of enterocyte layer migration in necrotizing enterocolitis.

2.1 INTRODUCTION

The ability of the cells that line the surface of the intestine to move plays a critical role in the ability of the body to heal any injury to the intestinal lining. The process by which such cells – called enterocytes –move is of great scientific interest. For example, there are certain conditions in which enterocyte migration is inhibited, therefore rendering the body susceptible to further injury and illness. One such condition is termed necrotizing enterocolitis (NEC), a disease that affects young babies and is characterized by impairment in the ability of enterocytes to move effectively, resulting in impaired healing (1-5). Mucosal healing also requires the generation of new enterocytes from precursors that are located deep within crypts of the mucosal lining, a process termed enterocyte proliferation (6). Enterocyte proliferation takes days before new cells are generated, as compared to enterocyte migration which may be completed within hours. Accordingly, it has become apparent that mucosal healing is largely determined by enterocyte migration (7), at least during the early phases. An understanding of the mechanisms

that govern enterocyte migration is therefore of vital importance in order to gain insights into the regulation of intestinal physiology during conditions of both health and disease. Importantly, little information exists to characterize the factors that regulate enterocyte migration under conditions that are associated with intestinal inflammation such as occurs in NEC.

Although many molecules may act in concert to inhibit enterocyte migration in the development of NEC, bacterial endotoxin (lipopolysaccharide, LPS) is likely to act as one of the earliest. LPS, which is found on the outer wall of gram negative bacteria, is a potent immunostimulant that exerts a large effect on the ability of enterocytes to migrate, given the large concentrations present within the lumen of the intestine. Mathematical modeling is emerging as an approach by which to address the complexity of inflammation in general (31) and of NEC in particular (30). To design experimental and mathematical models to predict the development of NEC, we therefore turned to an in vitro system in which small intestinal enterocytes (IEC-6 cells) were exposed to LPS at concentrations known to be present in the lumen of animals with experimental NEC (100ng/ml to 50μg/ml). The exposure of enterocytes to LPS in this concentration range leads to a profound, dose-dependent inhibition of enterocyte migration (8). Studies directed at elucidating the mechanisms that could mediate this migration inhibitory effect showed that LPS increases the adhesion of cells to the underlying matrix. This increased adhesion occurred due to a profound increase in the number of attachment sites – termed focal adhesions (8) – as well as an increase in the expression of binding receptors – called integrins – on the surface of the cell (9), in response to LPS.

The primary motivation for development of the model described herein is that the ability to predict the effect[s] of LPS and integrins on migration of enterocytes could have tremendous significance in understanding, and perhaps correcting, the factors leading to the defect in

mucosal healing that characterizes NEC. We give a mathematical description of the moving enterocyte layer and describe its properties by three constants related to the adhesion of cells to substrate, the elasticity of the layer, and the force exerted by lamellipodia, which are foot-like projections from the cell surface that allow the cell to move forward. We calibrate our model with real-time observations of cell migration and obtain estimates of these parameters. Finally, we find that with natural assumptions regarding the dependence of adhesion and lamellipod force on integrin concentration, the model yields results that are in qualitative agreement with experimental observations of the effect of adhesion on cell migration speed (10, 11).

2.2 THEORY AND METHODS

Existing mathematical models of wound healing are generally based on reaction-diffusion formalism in which moving edge of the cell layer is represented as a traveling wave of cell concentration. For adult epidermal wound healing, Sherratt and Murray (12) proposed a two-component model in which the epithelial layer is described by giving cell density per unit area and the time-dependence of this density is related to the concentration of the mitosis-regulating chemical. For embryonic epidermal wound healing Sherratt (13) developed a model involving actin filament network formation, based on a mechanochemical model for the deformation of epithelial sheets proposed by Murray and Oster (14). Recently Walker et al. (15, 16) used an agent-based model to simulate the wounded epithelial cell monolayers and suggested that simple rules are sufficient to qualitatively predict the calcium-dependent pattern of wound closure observed in vitro. In dermal wound healing, the mathematical model derived by Tranquillo and

Murray (17) includes the mechanism of dermal wound contraction. More complicated models including multiple cell types and multiple types or phases of the viscoelastic extracellular matrix (ECM) have been developed, some including additional equations for chemicals (such as growth factors) which modulate cell proliferative, motile and contractile behavior (18, 19). A detailed model of the dependence of cell speed on adhesion-receptor/ligand binding was proposed by DiMilla et al. (20).

In the present chapter, we focus on modeling the natural, unimpeded, cell migration during healing of the damaged intestinal mucosa. To design experimental and mathematical models to predict the development of the migration defect that characterizes NEC, the researchers in Dr. David Hackam's lab in University of Pittsburgh utilized a system in which small intestinal enterocytes (IEC-6 cells) are cultured on a glass coverslip, grown to confluence, and then scraped with a pipette or cell scraper to create a gap that represents the wound. The cells undergo motion, deformation, and proliferation. They have observed that the enterocyte cell layer is only one cell deep, and that during migration cells do not separate from the edge and no holes are formed in the interior of the layer. In addition, during migration cells at the edge and in the interior of the layer move generally toward the wound and never away from it (see Figure 2-4). Therefore, instead of a collection of diffusing cells, the cell layer can be described as an elastic continuum in which cells are connected, albeit loosely, to each other. The cells appear to move in accord with the so called 'sliding mechanism', in which cells in the interior respond passively to the pull of the cells at the edge (32,33,34).

2.3 MATHEMATICAL FORMULATION

The motion of cells is assumed to be driven by the cells at the edge of the wound through the formation of lamellipodia, which produce the driving force (22). The cells in the interior do not form lamellipodia and hence are not directly actuating the motion. However, they are tightly connected to the cells at the boundary. Tight junctions between the cells prevent separation (23) and hence the edge cells pull with them the cells in the interior of the layer. The cell layer stretches because of the tension applied by the edge cells, and the motion of the cells is slowed down by the adhesion between cells and the substrate.

The cell layer is represented by a one-dimensional elastic continuum capable of deformation, motion, and material growth (see Figure 2-1). Initially, the continuum is uniform and free from internal stresses. After part of the layer is scraped, a net external force F acting on the layer will develop at the resulting boundary as a result of lamellipod formation. This force, which will cause the layer to move and deform, will be opposed by the tension in the continuum resulting from stretching of the cells in the layer, and also by the adhesion between the continuum and the substrate during the motion.

Our model differs from published viscoelastic continuum models of epithelial sheets (17) in that we ascribe elasticity to the cell layer itself, but not to the substrate matrix. The forces considered in (17) are elastic forces and traction forces arising from the actin filament network between the cells and substrate that attaches to the cells. In our model, because we are concerned with in vitro experiments in which IEC-6 cells are planted on glass coverslips, we can safely ignore the elasticity of the substratum and only consider the forces coming from the lamellipod of the cells at edge and interaction between cells.

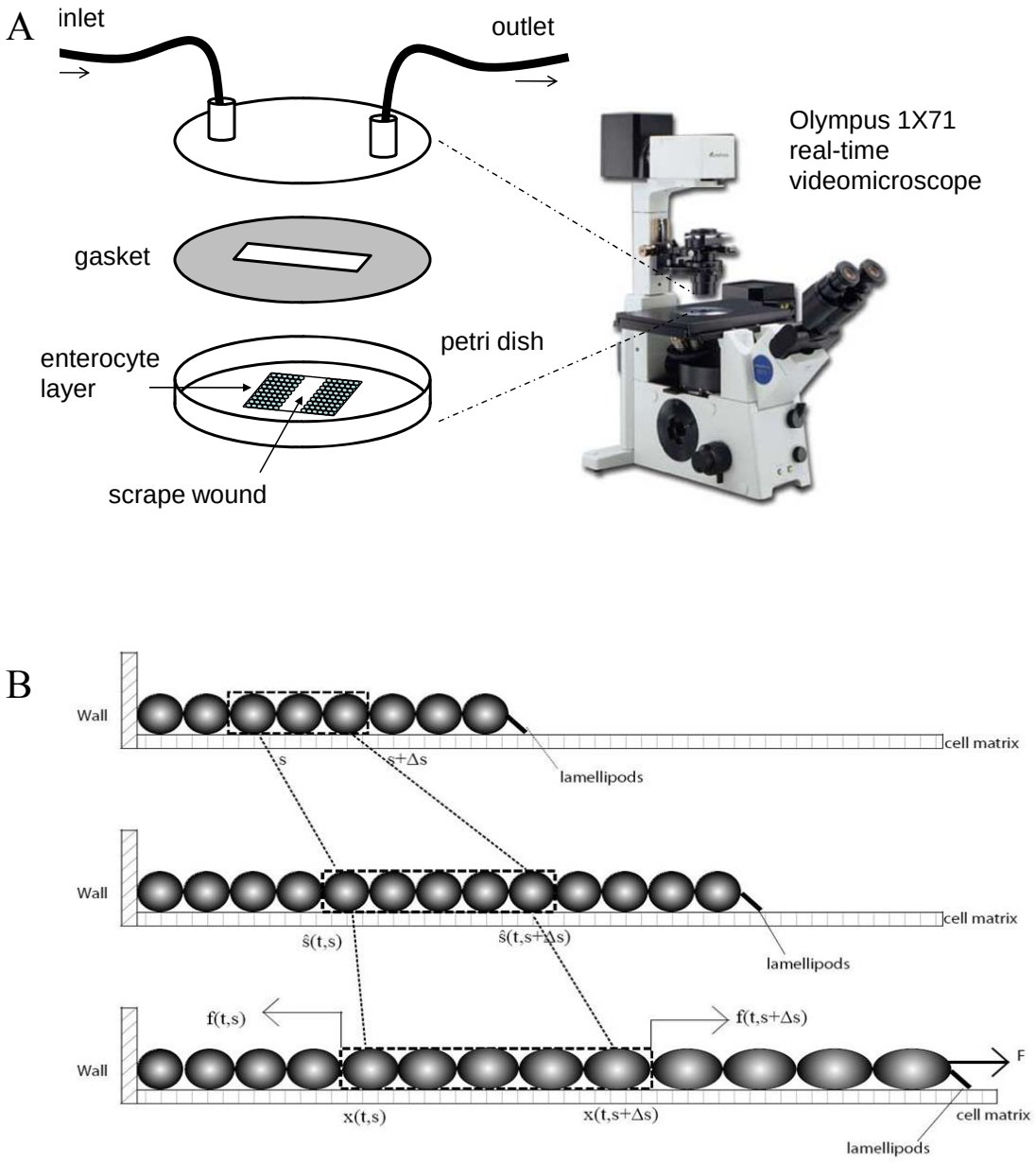

Figure 1

Figure 2-1: (A) Sketch of the experimental setup for monitoring in vitro mobility. Confluent IEC-6 cells were plated on glass coverslips, scraped with a cell scraper, and then mounted on the stage of an Olympus 1X71 inverted microscope warmed to 37°C. Fresh medium was continuously perfused across the cells. Differential interference contrast images were obtained every 5 min. (B) Schematic representation of the cell layer as one-dimensional continuum (only one side of the wound is shown): (i) Initial state. (ii) Hypothetical state at time t accounting for growth but not deformation. (iii) True configuration of the layer at time t

We employ the variable s to describe the position of a cell in the original layer. A proliferating cell generates two "offspring". We adhere to the convention that the offspring that is closer to the moving edge of the layer carries the s value of the original cell and we employ the variable $x(t,s)$ to denote the position of cell s in the layer at time t. In other words, $x(t,\sigma)$, $0 \le \sigma \le s$, is the position at time t of the offspring of cells originally located between 0 and s. In addition, we introduce the variable $\hat{s}(t,s)$ which describes the hypothetical position of cell s at time t if all deformation in the layer was instantaneously removed. Thus, $\hat{s}(t,\sigma)$, $0 \le \sigma \le s$, would be the position at t of the offspring of cells originally located between 0 and s if we accounted for growth but not deformation (see Figure 2-1).

Let us now consider a segment of cells which are the offspring of cells between s and $s+ds$ of the original layer with ds assumed small. At time t, such a segment extends between $x(t,s)$ and $x(t,s+ds)$, its velocity is $\dot{x}(t,s) = \partial x(t,s)/\partial t$, and acceleration $\ddot{x}(t,s) = \partial^2 x(t,s)/\partial t^2$. Balance of momentum implies that

$$M(t,s)\ddot{x}(t,s) + B(t,s)\dot{x}(t,s) = f(t,s+ds) - f(t,s) \qquad (2.1)$$

where $M(t,s)$ is the time-dependent mass of the segment, $B(s,t)$ is the coefficient describing the sliding resistance due to adhesion of the cells to the substrate, and f the resultant force on a cross-section of the layer.

It is reasonable to assume that the coefficient $B(s,t)$ is proportional to the extent of contact of the segment with the substrate (10,11) and hence

$$B(t) = \big(x(t,s+ds) - x(t,s)\big)b \qquad (2.2)$$

where b is the adhesion constant, which has the units of force times time divided by length squared. In addition, for slow motions one may neglect the acceleration term in Eq. 2.1 and hence, in view of Eq. 2.2, one obtains

$$\big(x(t,s+ds)-x(t,s)\big)b\dot{x}(t,s)=f(t,s+ds)-f(t,s) \tag{2.3}$$

which, in the limit $ds \to 0$, becomes,

$$b\frac{\partial x}{\partial s}\frac{\partial x}{\partial t}=\frac{\partial f}{\partial s} \tag{2.4}$$

The strain (deformation gradient) in the cell layer can be described by the quantity $\varepsilon = \partial x/\partial \hat{s} - 1$, with $\varepsilon > 0$ corresponding to stretch and $-1 < \varepsilon < 0$ corresponding to compression. The model must be completed by an appropriate choice of the constitutive relation describing the dependence of f on ε. When ε is small, one could assume that the resultant force is a linear function of the strain (Hooke's law):

$$f = k\varepsilon = k\left(\frac{\partial x}{\partial s}\left(\frac{\partial \hat{s}}{\partial s}\right)^{-1}-1\right) \tag{2.5}$$

Here the stretching modulus of the layer k has the unit of force as the cell-layer thickness is assumed constant. The drawback of Eq. 2.5 is that the resultant force (and hence the strain) remains finite if the material is compressed to infinitesimal volume. A more appropriate choice, which we make here, yields infinite magnitude of the resultant force for both $\varepsilon \to -1$ and $\varepsilon \to \infty$:

$$f = k\ln(\varepsilon+1) = k\left[\ln\left(\frac{\partial x}{\partial s}\right)-\ln\left(\frac{\partial \hat{s}}{\partial s}\right)\right] \tag{2.6}$$

(The difference between Eq. 2.5 and Eq. 2.6 is exhibited only when the cell layer is subjected to extreme deformation. We have verified that the choice of Eq. 2.5 instead of Eq. 2.6 would yield results essentially indistinguishable from those presented in this chapter.)

Any deformation of a cell is accompanied by an active remodeling of the cytoskeleton which generally results in a viscoelastic stress-strain response (24). In Eqs. 2.5 and 2.6 it is implicitly assumed that the stretching modulus k of the cell layer is time independent and hence

the cell layer responds instantaneously and passively to the forces generated on it. This assumption is made due to the fact that the timescale of the motion of the layer (~hours) is slow compared to the relaxation time of single-cell deformation which is of the order of tens of seconds (25). Therefore, one should think of k as the residual stretching modulus of the layer after cytoskeleton relaxation.

Material growth and decay of the layer can be described using the growth gradient $g(t,s) = \partial\hat{s}/\partial s$, which obeys

$$\frac{\partial g(t,s)}{\partial t} = \rho\, g(t,s) \tag{2.7}$$

where the growth rate ρ may generally depend on s, t but also ε or g itself. If one assumes that the growth rate is time and strain independent, the solution of Eq. 2.7 with initial condition $g(0,s) = 1$ is easily obtained as

$$g(t,s) = e^{\rho(s)t} \ . \tag{2.8}$$

From Eqs. 2.4, 2.6, 2.8 we obtain resulting equation:

$$\frac{\partial x}{\partial s}\frac{\partial x}{\partial t} = \frac{k}{b}\frac{\partial}{\partial s}\left(\ln\left(\frac{\partial x}{\partial s}\right) - \rho(s)t\right) \tag{2.9}$$

We assume that the location of the left boundary of the cell layer (at $s = 0$) is fixed while the right boundary (at $s = 1$ in dimensionless units) is free to move, and that the force applied at the right boundary is constant and equal to F. Thus, the initial and boundary conditions are, in view of Eq. 2.5,

$$\begin{aligned} x(0,s) &= s, && 0 \le s \le 1 \\ x(t,0) &= 0, && 0 \le t \\ \frac{\partial x(t,1)}{\partial s} &= e^{(F/k)+\rho(1)t}, && 0 < t \end{aligned} \tag{2.10}$$

Note that the constants b, k, and F appear in the problem only as the ratios $\kappa = k/b$

(units of length squared divided by time) and $\phi = F/k$ (dimensionless). The differential equation Eq. 2.9 with boundary and initial conditions Eqs. 2.10 can be solved numerically using finite difference methods (see *Appendix A*).

2.4 CONSTANT GROWTH RATE

If the growth rate ρ is spatially independent, the problem of Eqs. 2.9, 2.10 further simplifies as

$$\begin{aligned} \frac{\partial x}{\partial t} &= \kappa \frac{\partial^2 x}{\partial s^2}\left(\frac{\partial x}{\partial s}\right)^{-2} \\ x(0,s) &= s, \qquad && 0 \le s \le 1 \\ x(t,0) &= 0, && 0 \le t \\ \frac{\partial x(t,1)}{\partial s} &= e^{\phi+\rho t}, && 0 < t \end{aligned} \tag{2.11}$$

Figure 2-2 gives an example of the typical features of solutions of Eqs. 2.11 with a constant positive growth rate. The initial motion is dominated by the force applied by the lamellipodia on the edge of the layer. The velocity of the edge is decreasing as a result of increasing tension and increasing adhesion in the extended layer. The cells in the interior of the layer remain static for a time period proportional to their distance from the edge. At later times the motion of the layer becomes dominated by cell proliferation and the velocity of the edge increases again. The tensile strain decreases and eventually becomes positive. At this stage, the proliferation of new material, which pushes the old cells out of the way, is the driving force behind the motion of the layer.

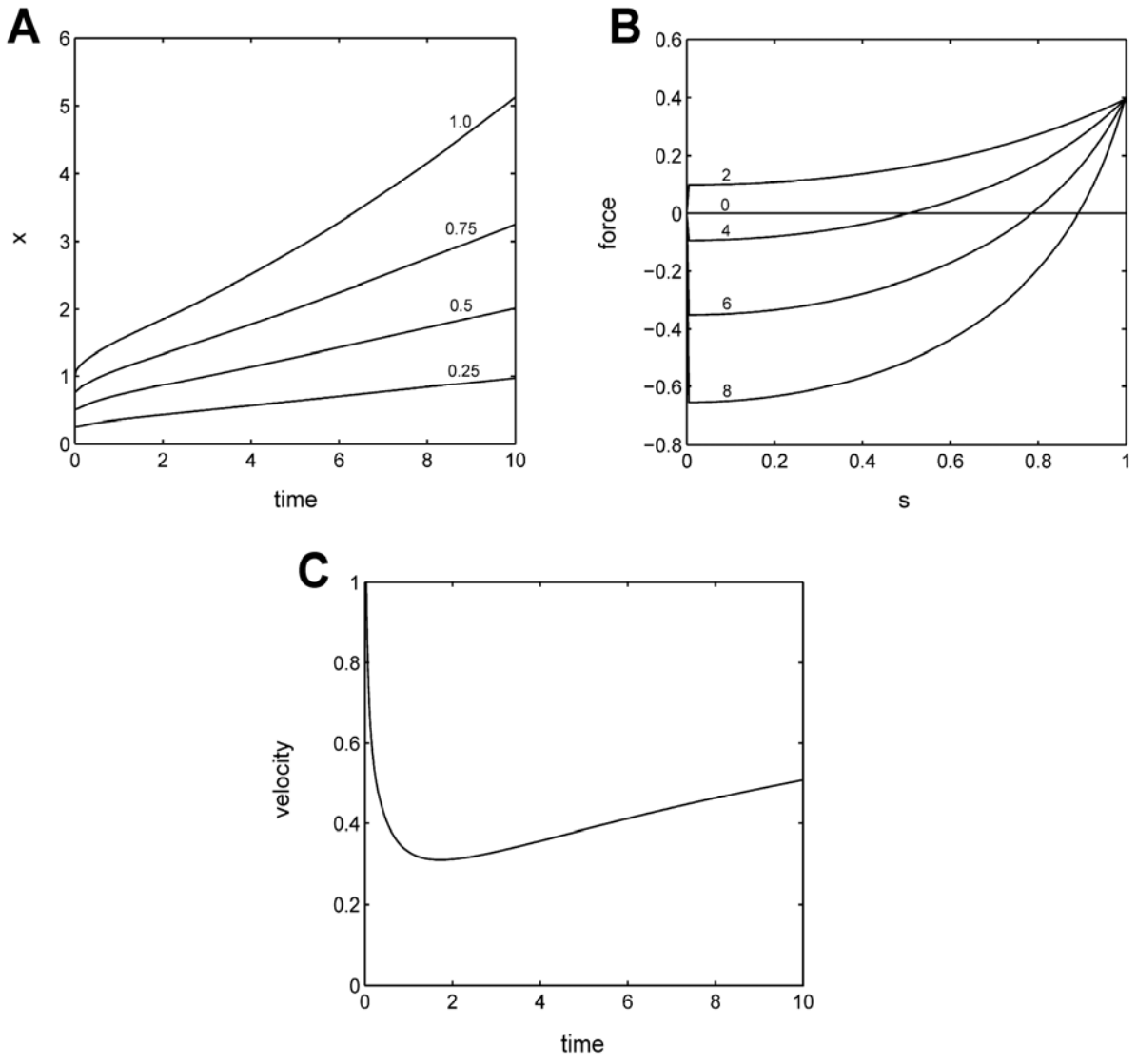

Figure 2-2: Generic behavior at constant proliferation rate. Here $\rho=0.2$, $\kappa=1$, and $\phi=0.4$. (A) Graphs of the position x of cells with s = 0.25, 0.5, 0.75, 1 as a function of time (in hours). (B) Resultant force f in the layer versus position s for t = 0, 2, 4, 6, 8 hr. (C) Velocity of the edge as a function of time (in hours).

2.5 CALIBRATION IN THE ABSENCE OF PROLIFERATION

In the case of migration of enterocytes on glass cover slips considered in this paper, we have observed that the proliferation rate is very low. In this case, ρ can be neglected and the problem Eqs. 2.11 becomes

$$\begin{aligned} \frac{\partial x}{\partial t} &= \kappa \frac{\partial^2 x}{\partial s^2}\left(\frac{\partial x}{\partial s}\right)^{-2} \\ x(0,s) &= s, \qquad 0 \le s \le 1 \\ x(t,0) &= 0, \qquad 0 \le t \\ \frac{\partial x(t,1)}{\partial s} &= e^{\phi} \qquad 0 < t \end{aligned} \tag{2.12}$$

The differential equation in Eq. 2.12 has an equilibrium (i.e., time-independent) solution $x(s) = e^{\phi} s$ that obeys the prescribed boundary conditions (but not the initial condition). This solution is a limiting case of the time-dependent solution and it implies that the maximum distance the right edge of the layer can reach is $x_{\max} = e^{\phi}$.

2.6 RESULTS

The parameters κ and ϕ of the model in Eq. 2.12 can be determined by calibration with experimental data obtained *in vitro*. In the experiment described in (5), IEC-6 cells were grown on glass coverslips to 100% confluence, serum-starved for 12 hours, scraped with a cell scraper,

and then transferred to the stage. Pictures were taken every five minutes for 17 hours to record the migration profiles of the cells. Figure 2-3 shows examples of such pictures. We used the recorded pictures of migrating cells to track the motion of selected ten cells located near the edges and in the interior of the layer. The cells are marked L1-L10 (in the lower layer) and U1-U10 (in the upper layer) (see Fig. 2-4). The distance traveled by the cells was measured in the direction perpendicular to the axis of the wound.

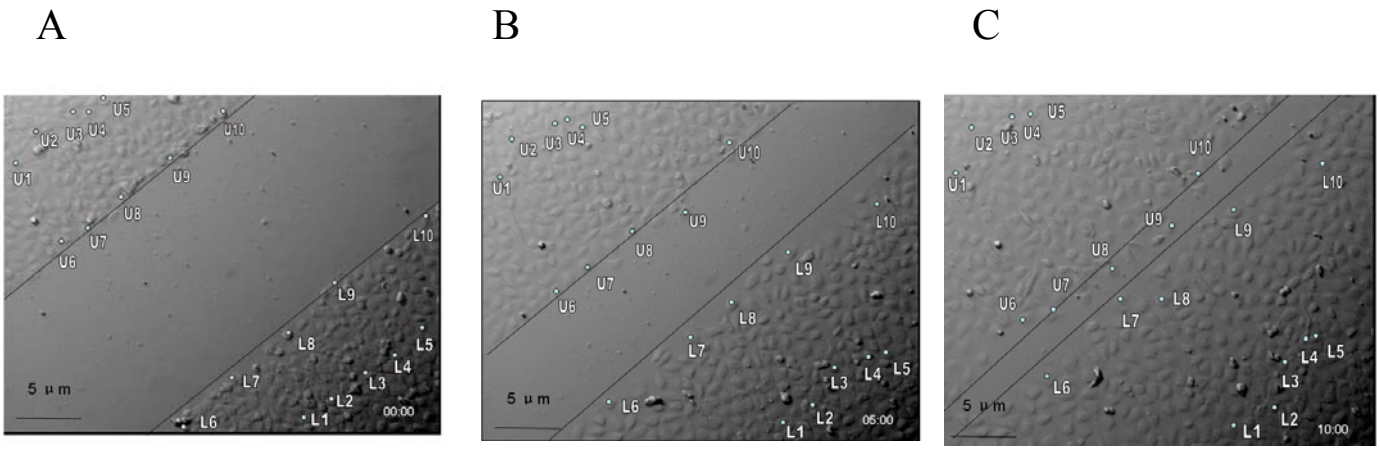

Figure 2-3: Snapshots of IEC-6 cells migrating on a glass cover slip at (A) t = 0, (B) t = 5h and (C) t = 10h. The tracked cells are labeled as U1…U10 and L1…L10 Snapshots of IEC-6 cells migrating on a glass cover slip at (A) t = 0, (B) t = 5h, and (C) t = 10h. The tracked cells are labeled as U1…U10 and L1…L10

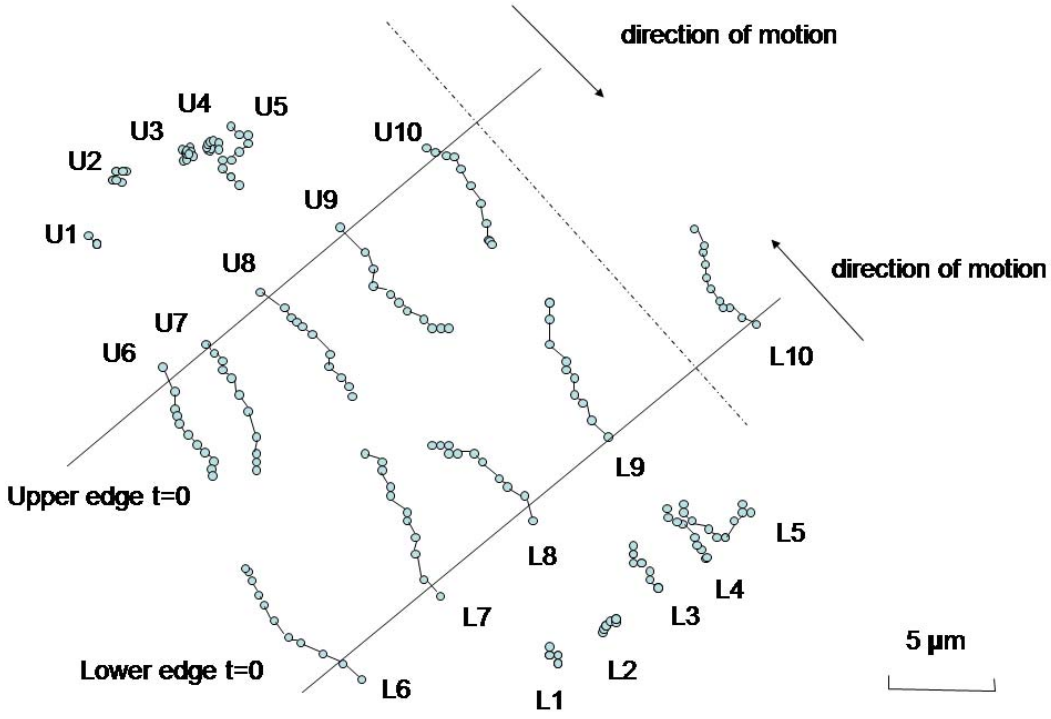

Figure 2-4: The observed paths of cells U1…U10 and L1…L10 of Figure 3. The positions of edges at t = 0 are indicated by solid lines. The direction of motion, along which traveled distances were measured, is shown as dash-dotted line.

From these measurements, we fit the average position of the group of cells L1-L5 in the interior of the lower layer and the group of cells L6-L10 near the edge. The model parameters were estimated using numerical solution of Eq. 12 and a routine nonlinear unconstrained minimization of the least square error. The distance of the wound edge from the fixed edge of the cell layer was assumed to be very large compared to the gap size and cell diameter. In our optimization code, we observed that the results are insensitive to this value (data not shown). The following values were obtained for the motion of the lower edge:

$\kappa = 5.92\ \mu m^2/hr,\ \phi = 0.86$

We repeated the data fitting for the upper layer where we averaged the position of cells U1-U5 located in the interior of the layer and the position of cells U6-U10 located near the edge.

We obtain the following values:

$\kappa = 3.87\ \mu m^2/hr,\ \phi = 1.04$

The averages over both layers are $\kappa = 4.9\ \mu m^2/hr$ and $\phi = 0.9$. As shown in Figure 2-5, the velocity of the cells at the edge is gradually decreasing while the velocity of cells in the interior of the layer is initially zero and then slowly increasing.

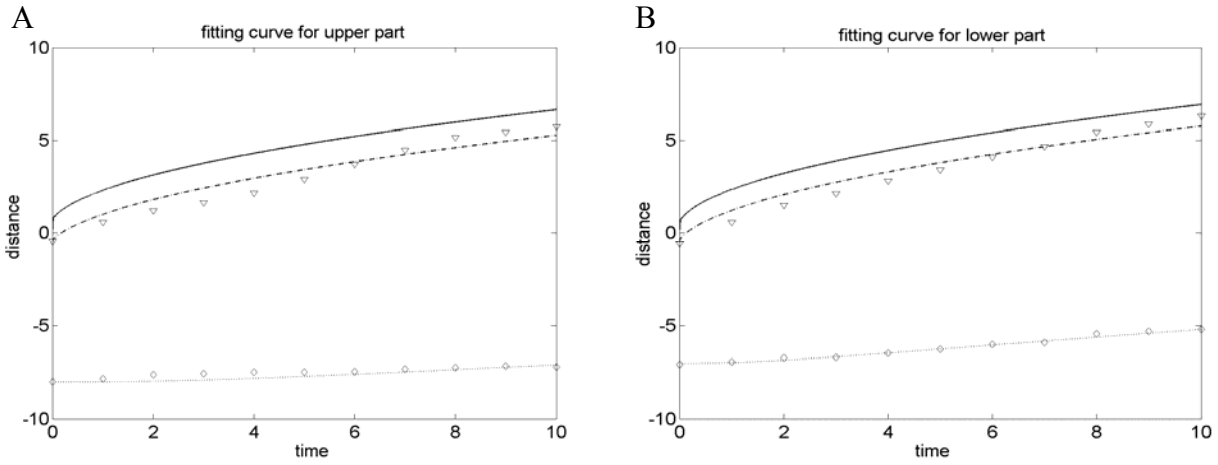

Figure 2-5: Dependence of traveled distance on time. Average distance traveled by cells in the direction perpendicular to the wound edge is shown as hollow diamonds (U1-U5 or L1-L5) and triangles (U6-U10 or L6-L10). Computed predictions are shown as solid (edge), dashed and dash-dotted curves.

2.7 DEPENDENCE OF MIGRATION ON INTEGRIN CONCENTRATION

The adhesion of cells to the substrate and the force exerted by lamellipodia are modulated by adhesion receptors, such as integrins, that connect the cell to the extracellular matrix. Integrin concentration and integrin-ligand affinity have been found to affect the speed of migrating cells (10).

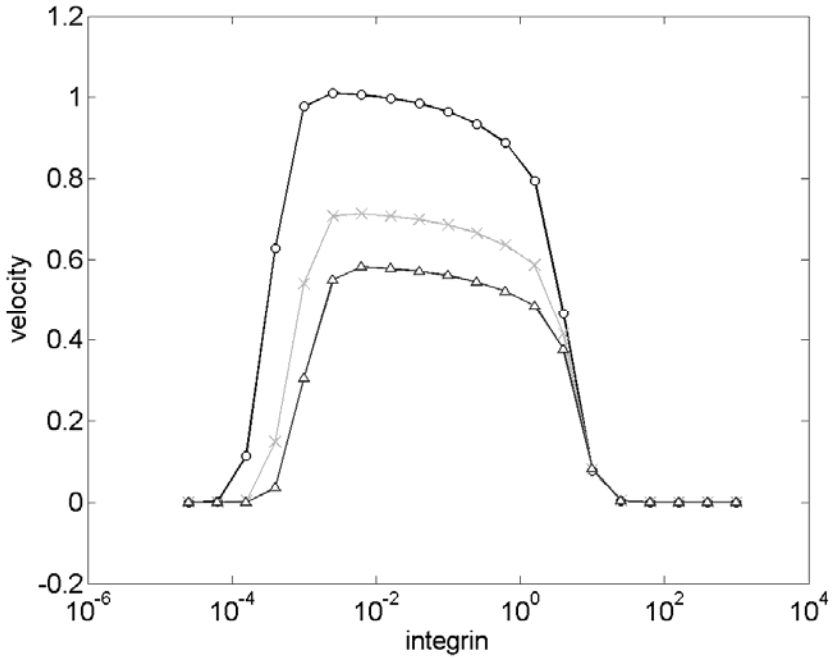

Figure 2-6: Dependence of edge migration velocity on integrin concentration for three different time instants: t = 2h (circles), t = 4h (crosses), t = 6h (triangles). Here $\rho = 0$, $\kappa = 4.90$, and $\phi = 1.16$.

The present model allows us to investigate the effect of integrins on migration speed by examining the dependence of the constants *b*, *k*, and *F* on integrin concentration *I*. At the present time this dependence is not known, however, the following assumptions appear reasonable: (i) the adhesion constant *b* should be proportional to *I*, (ii) the lamellipod force *F* should be proportional to $\sqrt{I}$, and (iii) the stretching modulus *k* of the layer should be independent of *I*. The difference in scaling between *b* and *F* stems from the fact that adhesion is generated on the entire cell-matrix contact surface, while the force of the lamellipod is only exerted at the cell edge. Since our one-dimensional model represents a two-dimensional layer of cells, *b* is proportional to the area of contact between the cell and the substrate while F is proportional to length of the cell edge. Remarkably, under these simple assumptions the graph of migration

velocity versus integrin concentration in Figure 6 shows the characteristic bell-shaped curve with low velocity corresponding to low or high integrin concentration and maximum velocity corresponding to intermediate integrin concentration (10,11). This observation is not meant to replace the detailed and quantitatively accurate model of the dependence of cell speed on adhesion (20), but rather to give some insight into the possible causes of observed velocity variability, such as may occur during inflammatory states.

2.8 DISCUSSION

The model developed in this paper accounts for the three effects influencing cell migration, i.e., the driving force of lamellipodia, the motion impeding adhesion between cells and the substrate, and the elasticity of the cell layer. In the case of constant proliferation, the model predicts increasing velocity of the wound edge. In the case of negligible proliferation the model predicts that the velocity of cells at the edge is initially greater and decreases with time, as is seen experimentally (26). This prediction differs dramatically from predictions of models based on reaction-diffusion equations in which the motion of the edge has constant or gradually increasing velocity. The velocity of cells in the interior of the layer is initially zero and then slowly increases, again in accord with observations. In contrast, none of the existing reaction-diffusion models makes predictions about the migration speed of cells in the interior of the layer.

One important consequence of the model is that in the absence of proliferation the maximum distance traveled by any edge is finite. It follows that if the gap of the wound is sufficiently large, the remaining enterocyte layer may not be able to close the wound. This

phenomenon was observed experimentally in studies of enterocytes cultured on glass coverslips (see Figure 2-7) and is not easily explained by a model based on reaction-diffusion equations.

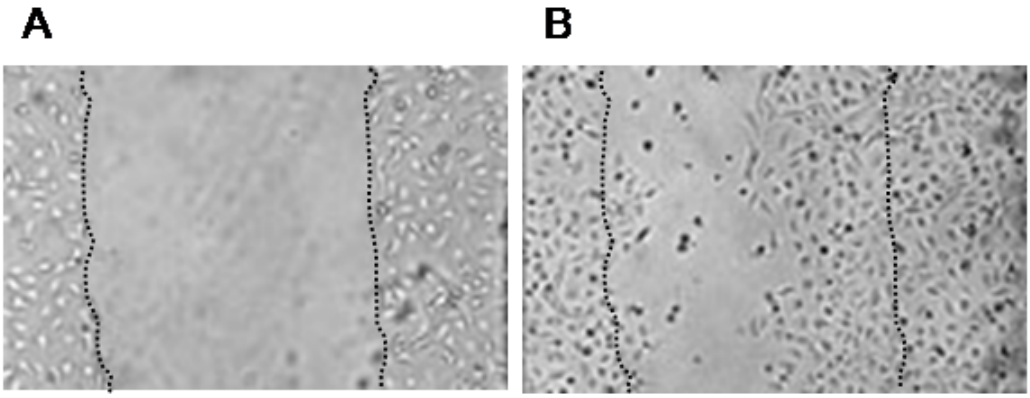

Figure 2-7: Enterocyte migration is incomplete under conditions of excessive wound formation. IEC-6 cells were plated on glass coverslips, scraped to induce a wound, then allowed to undergo wound closure over the ensuing 24h. The position of the wound edge at the beginning of the experiment (panel A) and 24 hours later (panel B) is indicated by the dotted line. In B the dark cells in the wound have undergone apoptosis.

At its present form the model yields ratios of the quantities of interest (κ characterizes the ratio of the stretching modulus k of the layer to the adhesion coefficient b, and ϕ is the ratio of the force F exerted by lamellipodia to the stretching modulus k) and hence the model enables us to make relative comparisons between these effects. In order to obtain true magnitudes of F, b, or k, one would need to perform an independent measurement of at least one of the three quantities. Prass et al. (27) have measured the cell stall force for keratinocytes using atomic force microscopy catilever and obtained a value ~40nN. If enterocytes migrating on glass coverslips exert similar force, then the corresponding value of the cell-layer stretching modulus k would be ~44 nN and adhesion/friction constant b would be ~0.11 hr·nN/μm^2.

Two different fits were performed in order to determine the coefficients κ and ϕ, one for the lower and one for the upper edge of the wound, yielding two different sets of parameters.

There are several possibilities as to likely sources of this difference. One possibility is that the cover slip was locally inhomogeneous in adhesion properties, which would have affected both κ and ϕ constants. Other sources of discrepancy could be local inhomogeneities in initial cell density or cell maturity.

The model described herein is sufficiently general in that it allows for more general growth rate laws to be incorporated. One extension would be to implement spatially variable growth rate $\rho(s)$. There are indications that the proliferation is increased in the area near the edge shortly after creation of the wound. Another possibility is to make growth rate dependent on the stretch in the layer - stretched layer may be more likely to reproduce than compressed, crowded one.

In summary, we have developed a simple model that accurately describes the migration of the enterocyte cell layer (both at the edge and in the interior) in terms of three characteristics: the adhesion of cells to substrate, the elasticity of the layer, and the force exerted by lamellipodia. Fitting of the model to measured data enables one to determine the magnitude of each of these characteristics as a function of the treatment conditions (such as the concentration of LPS).

It is important to point out that while the current model is clearly applicable to the situation of scrape wounding of enterocyte monolayers on glass coverslips *in vitro*, it also provides for useful – albeit partial - information regarding the applicability to *in vivo* wound healing. For instance, although wound healing *in vitro* occurs in three dimensions and may be influenced by the presence of inflammatory cells that could serve to modify the rate and extent of healing that occurs, the researchers in Dr. David Hackam's lab in University of Pittsburgh have recently demonstrated that the fundamental forces that drive wound healing within the intestine *in vivo* bear striking similarity to the *in vitro* situation described in the present study. The

similarities between *in vitro* migration of enterocytes and *in vivo* healing as occurs in NEC include a dependence on intact gap junction mediated cell-cell contacts for migration to occur (28), the inhibition of migration by inflammatory cytokines (e.g. IFN-γ) (28) and nitric oxide (29), and marked inhibition by pro-inflammatory macrophages that may be present within the sub-epithelial lamina propria (Anand et al, unpublished observations). Moreover, although proliferation of enterocytes must occur in order to replace cells that are lost due to damage, the role of enterocyte proliferation in the modulation of mucosal healing is significantly more important during chronic inflammatory states as opposed to the acute inhibition of healing as occurs during exposure to LPS (C. Leaphart et al, unpublished observations). Taken in aggregate, we submit that the current model provides important insights into enterocyte migration *in vitro* with useful correlates for the *in vivo* situation, both under basal conditions and during conditions of intestinal inflammation such as NEC.

3.0 TWO-DIMENSIONAL ELASTIC CONTINUUM MODEL OF ENTROCYTE LAYER MIGRATION

In this chapter, I present a two dimensional model based on the laws of continuum mechanics for the enterocyte layer migration.

3.1 INTRODUCTION

In the previous chapter, we developed a simple but accurate model that describes the migration of the enterocyte cell layer. A natural extension of it is to have a similar model but in higher dimension and incorporates the same effects (i) mobility promoting force due to lamellipod formation, (ii) mobility impeding adhesion to the cell matrix and (iii) elasticity of the cell layer. For the wound healing models, there exists a class of hyperbolic equation models which arise from mass conservation laws of densities of cells (36). This type of model is often used in the application of tumor growth modeling because the surface of the tumor is a free boundary and one seeks to determine both the tumor's region and the solutions of the differential equations within the tumor (37). Similarly, to model closure of wound by enterocytes migration, we consider the boundary of the wound be a moving boundary as well. Based on the laws of the continuum mechanics, we derived a two-dimensional model that incorporates the same effects as our 1d model. To numerically solve the resulting problem, we developed a computational

method based on the classical finite element method for parabolic equation. Although our method is limited for certain computational domain, it successfully produces the desired qualitative results.

3.2 MATHEMATICAL FORMULATION

We consider the enterocyte layer as a two-dimensional continuum. By the laws in continuum mechanics we have:

3.2.1 Conservation of Mass:

$$\frac{\partial \rho(\mathbf{x},t)}{\partial t} + \nabla \cdot (\rho \mathbf{v}) = g(\mathbf{A}(\mathbf{x},t)) \tag{3.1}$$

where ρ is the density of the cell, **v** represents the velocity at position **x.** The source term g is assumed to be zero because of absence of the proliferation,

3.2.2 Balance of Linear Momentum:

$$\rho \frac{\partial \mathbf{v}}{\partial t} + \rho(\mathbf{v} \cdot \nabla)\mathbf{v} = \rho \mathbf{f} + \nabla \cdot \mathbf{T} \tag{3.2}$$

The above equation is also called ***Cauchy's differential equation***. In our model, the body force **f**(**x**,t) is the result of the total friction on a material element exerted by the substrate and that is proportional to area:

$$\mathbf{f} = -\frac{b\mathbf{v}}{\rho} \tag{3.3}$$

3.2.3 Constitutive Equation

$$\mathbf{T} = -p\mathbf{I} \tag{3.4}$$

where **T** is the stress tensor. The pressure p can be both positive (when cells are compressed) or negative (when they are stretched).

For the dependence of pressure on cell density, we have the following different choices:

1) The linearized form of Hooke's law $p = -\kappa(\rho^{-1} - 1)$. It is appropriate for small changes in the density. The drawback of it is that the resultant stress remains finite if the material is compressed to infinitesimal volume.

2) The assumption from Ideal gas law $p = \kappa(\rho - 1)$. It works for large density of the cell layer but is not good for small density. If the material stretches to infinite volume, the tension within the cells should go to infinite and it is clear that this assumption does not have this feature.

3) The following relation $p = \kappa \ln(\rho)$ is good for both large and small density. It yields infinite magnitude of the resultant stress for both infinitesimal and infinite volume.

Moreover, as we shall see below, this choice leads to the standard moving boundary problem for heat equation, the Stephan problem.

After we plug it into Eq 3.4 and it becomes:

$$\mathbf{T} = -\kappa \ln(\rho)\mathbf{I} \tag{3.5}$$

Then we combine Eq. 3.2, Eq. 3.3 and Eq. 3.4 together, we get:

$$\rho \frac{\partial \mathbf{v}}{\partial t} + \rho(\mathbf{v} \cdot \nabla)\mathbf{v} = -\rho \frac{b\mathbf{v}}{\rho} - \nabla(\kappa \ln(\rho)) \tag{3.6}$$

After neglecting the material time derivative of the velocity, i.e., letting $\rho\frac{\partial \mathbf{v}}{\partial t}+\rho(\mathbf{v}\cdot\nabla)\mathbf{v}=0$, Eq. 3.6 becomes:

$$b\mathbf{v}=-\nabla(\kappa\ln(\rho)) \tag{3.7}$$

Because the source term g in Eq. 3.1 is zero, Eq. 3.1 becomes.

$$\frac{\partial\rho(\mathbf{x},t)}{\partial t}=-\nabla\cdot(\rho\mathbf{v}) \tag{3.8}$$

Thus we obtain Eq 3.7 and Eq. 3.8 that are analogous to Darcy's law in the theory of flow through porous media.

Let $k=\kappa/b$ and plugging Eq. 3.7 into Eq. 3.8, we get our two-dimensional elastic continuum model:

$$\frac{\partial\rho(\mathbf{x},t)}{\partial t}=k\nabla\cdot(\nabla\rho) \tag{3.9}$$

To reduce it to our one-dimensional model, we have $\rho=(\frac{\partial x}{\partial s})^{-1}$ and $v=\frac{\partial x}{\partial t}$. After putting them into Eq. 3.7, we have

$$b\frac{\partial x}{\partial t}=-\nabla(\kappa\ln((\frac{\partial x}{\partial s})^{-1}))=-\kappa\frac{\partial x}{\partial s}\frac{\partial s}{\partial x}\frac{\partial}{\partial s}(\frac{\partial x}{\partial s})^{-1}=\kappa(\frac{\partial x}{\partial s})^{-2}\frac{\partial^2 x}{\partial s^2}$$

that is same as the Eq.2.11.

3.2.4 Moving boundary initial value problem for heat equation

$$\frac{\partial\rho}{\partial t}=\nabla\cdot k\nabla\rho \tag{3.10}$$

To be general, we assume the initial density of tissue equals one on the initial domain.

Initial Condition: $\rho(\mathbf{x},0)=1$ on Ω^0

On the exterior boundary $\partial\Omega_2^t$ (see Figure 3-1), we assume the domain is fixed and there is no in-flux for the cell. We note that this is agreed with the experiment setting. On the interior moving boundary $\partial\Omega_1^t$, we assume the lamellipodia exerts a constant force –F (the negative sign means the force is outward and the cells are stretched). By Eq. 3.4 and our choice of dependence of pressure $p=\kappa\ln(\rho)$, we get the boundary condition $\rho=e^{F/\kappa}$ on $\partial\Omega_1^t$. To reduce the number of parameters, we assume b=1, thus $k=\kappa$.

Boundary Condition: $\nabla\rho\cdot\mathbf{n}=0$ on $\partial\Omega_2^t$

$\rho=e^{F/k}$ on $\partial\Omega_1^t$

On the moving boundary $\partial\Omega_1^t$, by Eq. 3.7, we have

$$b\mathbf{v}=-\nabla(\kappa\ln(\rho))=-\nabla(\kappa\frac{1}{\rho_{\partial\Omega_1^t}}\nabla\rho)=-\nabla(\kappa e^{-F/k}\nabla\rho) \qquad (3.11)$$

We then derive the following equation.

Thus, the motion of the boundary obeys the following condition.

Stephan Condition: $v\cdot\mathbf{n}=ke^{-F/k}\nabla\rho\cdot\mathbf{n}$ on $\partial\Omega_1^t$

The vector **n** is the unit outward normal to $\partial\Omega_1^t$.

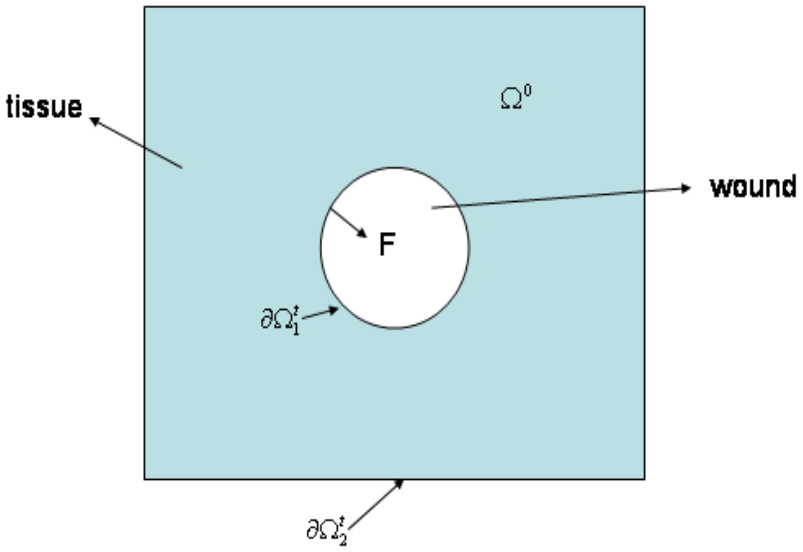

Figure 3-1: Computational domain of moving boundary initial value problem Eq. 3.10

3.3 NUMERICAL METHOD

Not like the classical heat equation, which is solved in the fixed domain, the boundary of our problem Eq. 3.10 is nonstationary. To determine the computational domain every time step, we can use its velocity from previous time step and solve the equation on its latest domain. Based on this idea, we develop a modified Finite Element Method to solve this problem.

3.3.1 Finite Element Method (FEM) for parabolic equation on fixed domain

3.3.1.1 Introduction

The finite element method originated from solving for problems in the civil engineering and aeronautical engineering (39). Although there are many different types of FEM existing now, the essential characteristic of it is the mesh discretization of a continuous domain into a set of discrete sub-domains. Let us consider the standard parabolic equation that arises from our moving boundary problem Eq. 3.10:

$$\frac{\partial \rho}{\partial t} = \nabla \cdot k \nabla \rho \qquad \text{in } \Omega$$

Initial Condition $\rho(\mathbf{x},0) = 1$

Boundary Condition: $\nabla \rho \cdot \mathbf{n} = 0$ on $\partial\Omega_2$ (3.12)

$\rho = e^{F/k}$ on $\partial\Omega_1$

where Ω is a fixed convex domain in R^2 with smooth boundary $\partial\Omega = \partial\Omega_1 \cup \partial\Omega_2$. The vector **n** is the unit outward normal to $\partial\Omega$.

3.3.1.2 Semidiscrete Galerkin approximation

Definition: Hilbert Spaces $H^m(\Omega)$

First we introduce the vector space of square integrable functions on Ω ,

$$L_2(\Omega) \equiv \{u \,|\, \|u\|_0 = [\int_\Omega u^2 dx]^{1/2} < \infty\}$$

$$H^m(\Omega) \equiv \{u \in L_2(\Omega) \,|\, D^\alpha u \in L_2(\Omega), 0 \le |\alpha| \le m\}$$

The initial-boundary value problem Eq. 3.12 can be replaced by the following equivalent *Galerkin problem*. Find a function $\rho(\mathbf{x},t)$, continuously differentiable with respect to t, such that $\rho \in S$ and for all $v \in S_0$, we have

$$\int_\Omega \rho_t v d\mathbf{x} + \int_\Omega k\nabla\rho \cdot \nabla v d\mathbf{x} = 0 \tag{3.13}$$

Where S is the set of functions:

S= $\{v|$ for each $0 < t \le T, v(\cdot,t) \in H^1(\Omega)$ and $v_t(\cdot,t) \in L^2(\Omega)$; and $v(\mathbf{x},t)=e^{F/k}$ on $\partial\Omega_1\}$ and $S_0 = \{$ $v \in H^1(\Omega) | v(\mathbf{x}) = 0$ on $\partial\Omega_1\}$.

The solution to the Galerkin problem is also a solution of the initial-boundary value problem Eq 3.12. The converse requires a solution to the Galerkin problem to have additional smoothness.

We choose a finite-dimensional subspace $S^h \subset S_0$ spanned by $\{\phi_i : 1 \le i \le N\}$. Here h is a mesh gauge that approaches 0 as $N \to \infty$ and in our computation, we choose the triangular mesh and the basis function $\{\phi_i\}$ be the piecewise linear functions i.e. $\phi_i = 1$ at node $\mathbf{x}_i$ and zero elsewhere. Since we have Dirichlet boundary condition on $\partial\Omega_1$, we have the following *semidiscrete Galerkin approximation* $u(\mathbf{x},t)$ to $\rho(\mathbf{x},t)$.

$$u(\mathbf{x},t) = \sum_{i=1}^{N} c_i(t)\phi_i(\mathbf{x}) + \sum_{i=N+1}^{N+p} e^{\frac{F}{\kappa}}\phi_i(\mathbf{x}) \tag{3.14}$$

Where $\{\phi_i\}$ with $N+1 \le i \le N+p$ is the basis function for node $\mathbf{x}_i$ on $\partial\Omega_1$. The coefficients $c_i(t)$ are continuously differentiable functions of t on [0, T] and can be determined by the system of equations:

$$\int_\Omega u_t \phi_i d\mathbf{x} + \int_\Omega k\nabla u \cdot \nabla\phi_i d\mathbf{x} = 0, \qquad 1 \le i \le N \tag{3.15}$$

Substituting Eq. 3.14 into Eq. 3.15 gives a system of ordinary differential equations:

$$\mathbf{M}\frac{d\mathbf{C}}{dt}+\mathbf{KC}=\mathbf{F} \tag{3.16}$$

where the N x N mass matrix is:

$$\mathbf{M}_{i,j}\equiv\int_{\Omega}\phi_i(\mathbf{x})\phi_j(\mathbf{x})d\mathbf{x} \tag{3.17}$$

the N x N stiffness matrix is:

$$\mathbf{K}_{i,j}\equiv\int_{\Omega}k\nabla\phi_i(\mathbf{x})\cdot\nabla\phi_j(\mathbf{x})d\mathbf{x} \tag{3.18}$$

the N x 1 source vector is:

$$\mathbf{F}_j\equiv -k\int_{\Omega}\sum_{i=N+1}^{N+p}e^{\frac{F}{k}}\nabla\phi_i(\mathbf{x})\cdot\nabla\phi_j(\mathbf{x})d\mathbf{x} \tag{3.19}$$

and the N x 1 vector of unknows:

$$\mathbf{C}(t)=[c_i(t)]^T \tag{3.20}$$

3.3.1.3 Complete discretization

Let $\Delta t=\frac{T}{N}>0$ be the time step and solution **C**(t) at $t_m=m\Delta t$ (m=1,2,..N) be $\mathbf{C}^m$. The backward difference approximation of $\frac{d\mathbf{C}}{dt}$ at t_m is defined as:

$$\frac{\mathbf{C}^m-\mathbf{C}^{m-1}}{\Delta t} \tag{3.21}$$

Plugging Eq. 3.21 into Eq. 3.16 and evaluating **C**(t) at t_m, we get the following Backward Euler approximation of Eq. 3.16:

$$\mathbf{M}\left(\frac{\mathbf{C}^m - \mathbf{C}^{m-1}}{\Delta t}\right) + \mathbf{K}\mathbf{C}^m = \mathbf{F} \tag{3.22}$$

Rearranging the items of Eq. 3.22, we have:

$$\mathbf{C}^m = (\mathbf{K} + \mathbf{M}/\Delta t)^{-1}(\mathbf{F} + \mathbf{M}/\Delta t\mathbf{C}^{m-1}) \tag{3.23}$$

3.3.1.4 Convergence of the semidiscrete solution

In this section, we establish convergence of the semidiscrete Galerkin approximation $u(\mathbf{x},t)$ to the true solution $\rho(\mathbf{x},t)$. Since we let $S^h \subset S_0$ be a space of continuous, piecewise linear functions, we can choose the piecewise linear interpolant $\tilde{u}(\mathbf{x},t)$ be an approximation to $\rho(\mathbf{x},t)$ (40). Further assume the initial condition that $\tilde{u}(\mathbf{x},0) = u(\mathbf{x},0) = \rho(\mathbf{x},0)$.

Assume that $$\tilde{u}(\mathbf{x},t) = \sum_{i=1}^{N} \tilde{c}_i(t)\phi_i(\mathbf{x}) + \sum_{i=N+1}^{N+p} e^{\frac{F}{k}}\phi_i(\mathbf{x}) \tag{3.24}$$

Define for $1 \le i \le N$,

$$k_i(t) \equiv \int_\Omega \tilde{u}_t \phi_i d\mathbf{x} + \int_\Omega k\nabla\tilde{u}\cdot\nabla\phi_i d\mathbf{x} \tag{3.25}$$

Let $v = \phi_i$ in Eq. 3.13. Subtracting Eq. 3.13 from Eq. 3.25, we have

$$k_i(t) \equiv \int_\Omega (\tilde{u} - \rho)_t \phi_i d\mathbf{x} + \int_\Omega k\nabla(\tilde{u} - \rho)\cdot\nabla\phi_i d\mathbf{x} \tag{3.26}$$

and subtracting Eq. 3.14 from Eq. 3.25, we obtain:

$$k_i(t) \equiv \int_\Omega (\tilde{u} - u)_t \phi_i d\mathbf{x} + \int_\Omega k\nabla(\tilde{u} - u)\cdot\nabla\phi_i d\mathbf{x} \tag{3.27}$$

Now let $V_1 \equiv \tilde{u} - \rho$ and $V_2 \equiv \tilde{u} - u = \sum_{i=1}^{N} \varepsilon_i(t)\phi_i(\mathbf{x})$, where $\varepsilon_i = \tilde{c}_i - c_i$. Multiply Eq. 3.26 and Eq. 3.27 by $\varepsilon_i(t)$ and sum on i, we have

$$\sum_{i=1}^{N} \varepsilon_i(t)k_i(t) = \int_\Omega V_{1t}V_2 d\mathbf{x} + \int_\Omega k\nabla V_1\cdot\nabla V_2 d\mathbf{x} \tag{3.28}$$

and

$$\sum_{i=1}^{N} \varepsilon_i(t) k_i(t) = \int_\Omega V_{2t} V_2 d\mathbf{x} + \int_\Omega k \nabla V_2 \cdot \nabla V_2 d\mathbf{x} \tag{3.29}$$

Let Eq. 3.28 equals to Eq. 3.29, we have:

$$\int_\Omega V_{1t} V_2 d\mathbf{x} + \int_\Omega k \nabla V_1 \cdot \nabla V_2 d\mathbf{x} = \int_\Omega V_{2t} V_2 d\mathbf{x} + \int_\Omega k \nabla V_2 \cdot \nabla V_2 d\mathbf{x}$$

$$\leq \frac{1}{2}\|V_{1t}\|_0^2 + \frac{1}{2}\|V_2\|_0^2 + \frac{1}{2}\left\|k^{1/2}\nabla V_1\right\|_0^2 + \frac{1}{2}\left\|k^{1/2}\nabla V_2\right\|_0^2 \tag{3.30}$$

We use the inequality $ab \leq \frac{1}{2}a^2 + \frac{1}{2}b^2$ to obtain the inequality in Eq. 3.30. Furthermore, using the equalities:

$$\int_\Omega V_{2t} V_2 d\mathbf{x} = \frac{1}{2}\frac{d}{dt}\int_\Omega {V_2}^2 d\mathbf{x} = \frac{1}{2}\frac{d}{dt}\|V_2\|_0^2$$

We can rewrite Eq. 3.30 as:

$$\frac{d}{dt}\|V_2\|_0^2 + \left\|k^{1/2}\nabla V_2\right\|_0^2 \leq \|V_2\|_0^2 + \|V_{1t}\|_0^2 + k\|\nabla V_1\|_0^2 \tag{3.31}$$

or

$$\frac{d}{dt}\|V_2\|_0^2 - \|V_2\|_0^2 + \left\|k^{1/2}\nabla V_2\right\|_0^2 \leq \|V_{1t}\|_0^2 + k\|\nabla V_1\|_0^2$$

Integrating over t and by Gronwall's lemma, we have

$$\begin{aligned} &\|\tilde{u} - u\|_0^2 + \int_0^t \left\|k^{1/2}\nabla(\tilde{u} - u)\right\|_0^2 ds \equiv \\ &\|V_2\|_0^2 + \int_0^t \left\|k^{1/2}\nabla V_2\right\|_0^2 ds \leq K\int_0^t \|V_{1t}\|_0^2 + \|\nabla V_1\|_0^2 ds \end{aligned} \tag{3.32}$$

Theorem. Let $\rho(\mathbf{x}, t)$ be the solution to the parabolic initial-boundary value problem Eq.3.12 and for each t let $u(\cdot, t)$ be its semidiscrete Galerkin approximation. Assume that for each t,

$\rho(\mathbf{x},t)$ and $\rho_t(\mathbf{x},t)$ belong on $H^{2n}(\Omega)$ (n=2 for our two-dimensional case). The interpolant $\tilde{u}(\cdot,t)$ of ρ is in the form Eq. 3.24, such that

$$\left\|\rho-\tilde{u}\right\|_m \equiv O(h^{2n-m}), \qquad \text{m=0,1} \qquad (3.33)$$

as $h \to 0$, then for $0 \le t \le T$,

$$\left\|k^{1/2}\nabla(\rho-u)\right\|_0 \le Kh^{2n-1} \qquad (3.34)$$

where K depends on T and ρ.

Proof: By the triangle inequality,

$$\left\|k^{1/2}\nabla(\rho-u)\right\|_0 \le \left\|k^{1/2}\nabla(\rho-\tilde{u})\right\|_0 + \left\|k^{1/2}\nabla(\tilde{u}-u)\right\|_0$$

By Eq. 3.33, the first term on the right is $O(h^{2n-1})$. For the second term, it is bounded by the square root of the right side of Eq. 3.32.

Furthermore, since $\tilde{u}_t$ is the interpolant of ρ_t and Eq. 3.33 holds also for $\left\|\rho_t-\tilde{u}_t\right\|_m$, we have

$$\left\|V_{1t}\right\|_0^2 \equiv O(h^{4n})$$

Thus substituting it into Eq. 3.32, we have that for fixed t,

$$\left\|k^{1/2}\nabla(\rho-u)\right\|_0 = \left\|k^{1/2}\nabla V_2\right\|_0 \le O(h^{2n-1})$$

3.3.2 Algorithm

3.3.2.1 Main procedure

Because our problem has the time-dependent boundary, we can not apply the standard finite element method for the parabolic equation directly. In order to solve this moving boundary

problem, we design the following computation method: (See Figure 3-2 for general procedure and Table 3-1 for details).

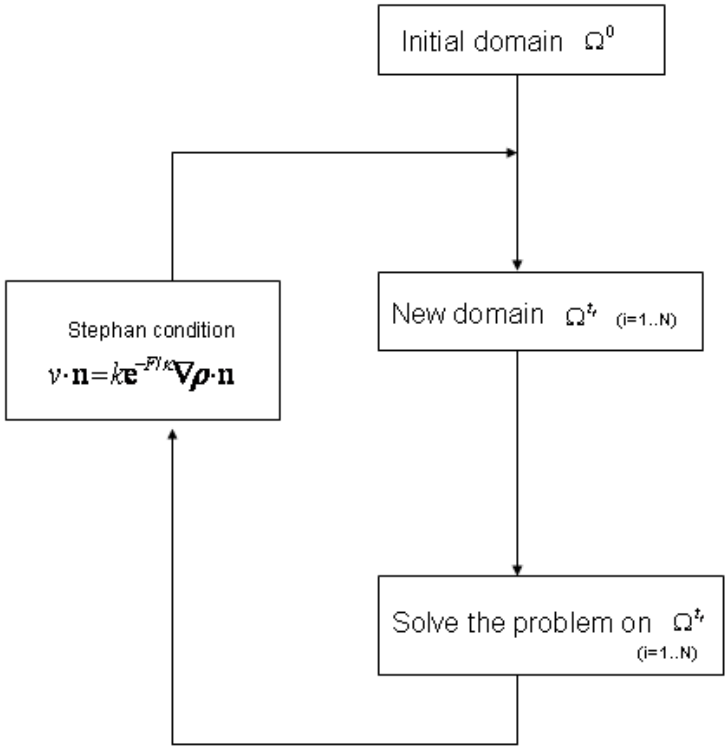

Figure 3-2: The general computation procedure for solving the moving boundary initial value problem Eq. 3.10

Table 3-1: The details of the algorithm for computing moving boundary initial problem Eq. 3.10

1. Get the initial mesh M(0) on the initial domain Ω^0 by using MATLAB mesh generator DistMesh (41).

2. Get new mesh M(i) at time step i, $i \geq 1$

2.1 Calculate $\nabla\rho$ on the triangles along the moving boundary $\partial\Omega_i^i$
2.2 Calculate the velocity on these triangles by using Stephan condition: $v\cdot\mathbf{n}=ke^{-F/k}\nabla\rho\cdot\mathbf{n}$
2.3 Get new mesh points and generate new mesh M(i), $i \geq 1$ (See next section for details)

3. Solve solution on the new mesh M(i)

3.1 Set solution **C**(i) equal $e^{-F/k}$ on the new moving boundary.
3.2 Get the Mass Matrix **M**, Stiff Matrix **K** and source vector **F** by using MATLAB routine "assema.m"
3.2 Solve solution **C**(i+1) by Backward Euler Method: $$\mathbf{C}(i+1)=(\mathbf{K}+\mathbf{M}/\Delta t)^{-1}(\mathbf{F}+\mathbf{M}/\Delta t\mathbf{C}(i))$$
3.3 Goto 2

3.3.2.2 How to get new mesh M(i)

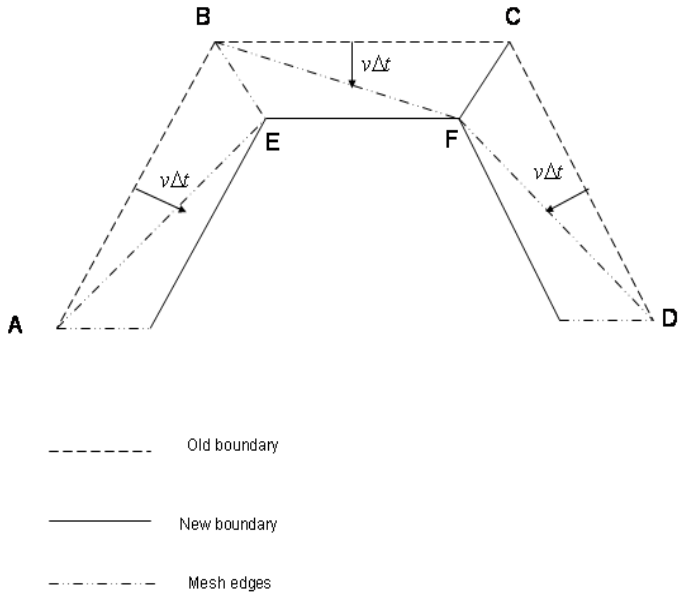

Figure 3-3: The diagram that shows how to obtain the new mesh M(i) at time step i. A,B,C and D are the mesh points on the moving boundary of mesh M(i-1). E and F are the new mesh points.

This figure above shows how we get the new mesh M(i) at time step i. For instance, we consider the mesh points A, B and C on the moving boundary of M(i-1). By moving AB and BC parallel in the normal direction of their velocities and by $v\Delta t$ units, we can solve their intersection point E which is also the new mesh point. Similarly we can get the new mesh point F. But for a special case (See Figure 3-4), if AB and CD intersect before they intersect with BC, we have to merge the mesh points E and F. By connecting the new mesh points E and F (Figure 3-3) or E (Figure 3-4) to their corresponding old mesh points A,B,C and D and repeating the same procedure for all the mesh points on the moving boundary of M(i-1), finally we obtain the new mesh M(i).

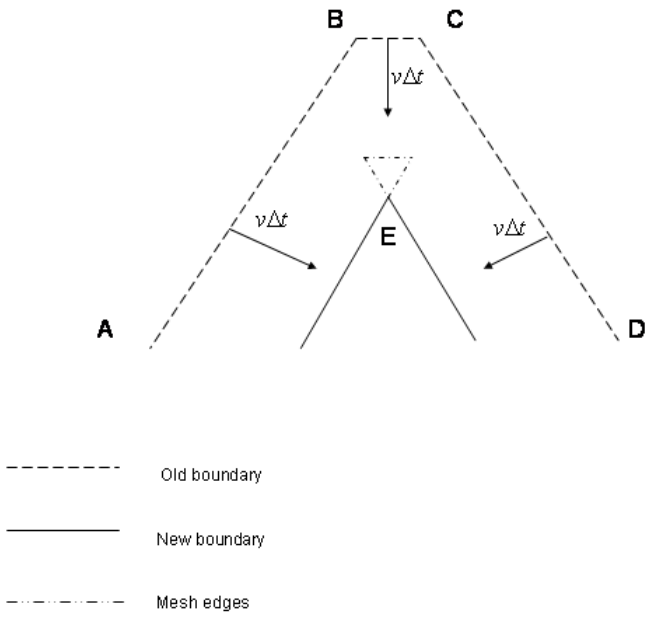

Figure 3-4: The diagram that shows a special case of how to obtain the new mesh M(i) at time step i. A,B,C and D are the mesh points on the moving boundary of mesh M(i-1). E is the new mesh points.

3.4 NUMERICAL RESULTS:

The following are the computation results:

A

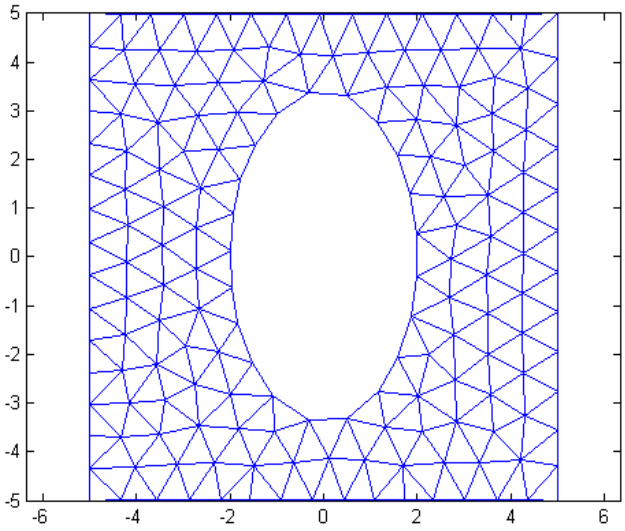

B

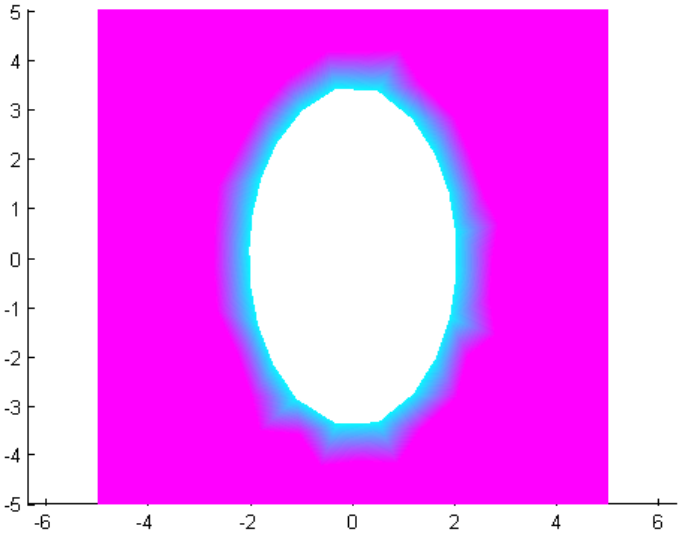

Figure 3-5: (A) The initial finite element triangular mesh M(0) of Eq. 3.10 in ellipse domain. (B) The initial solution of Eq. 3.10 with F=1 and k=1.

A

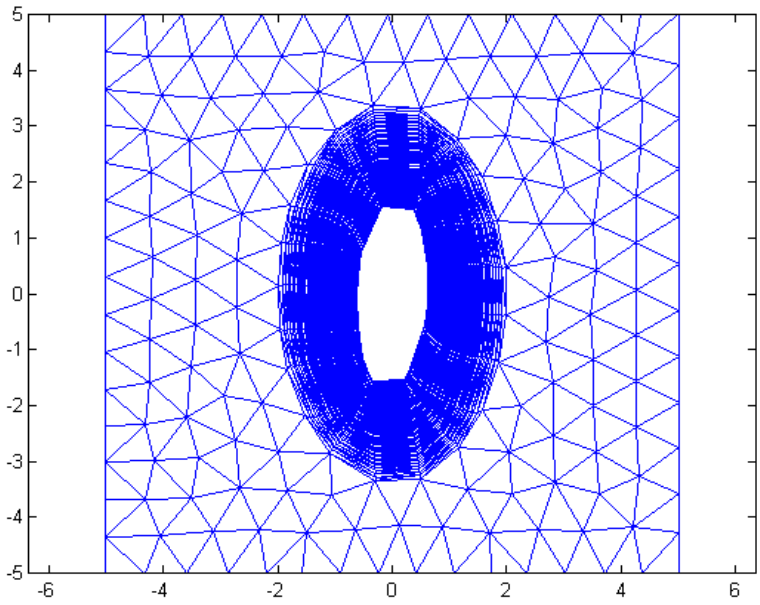

B

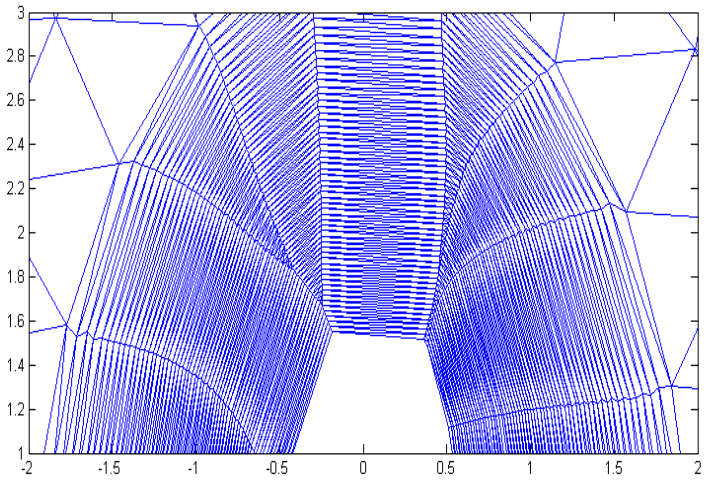

Figure 3-6: (A) The finite element mesh M(i) at time step i, where i=100, T=2 and $\Delta t = \frac{T}{100}$. (B) The initial solution of Eq. 3.10 with F=1 and k=1.

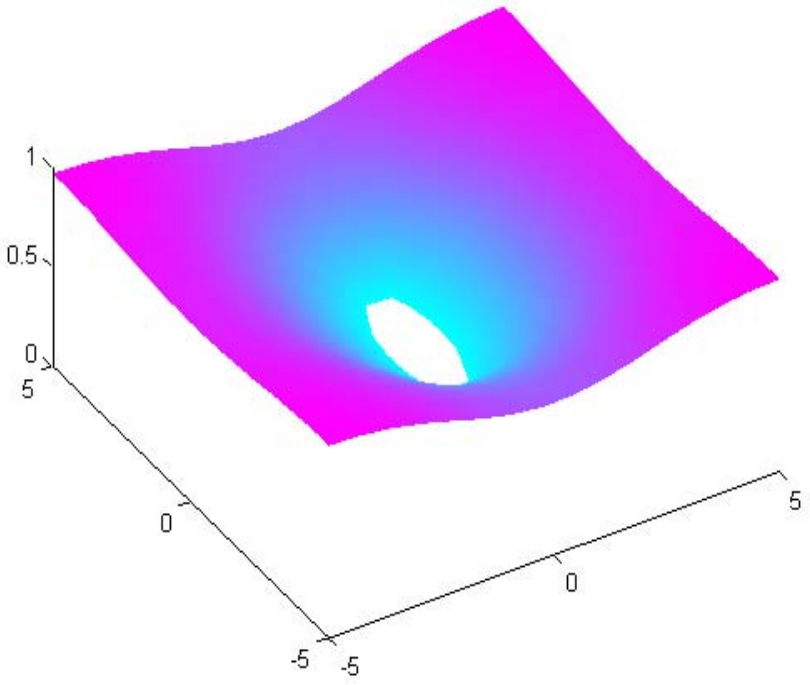

Figure 3-7: The plot of solution of Eq. 3.10 at t=2 with $\Delta t = \frac{1}{50}$, F=1 and k=1.

3.5 DISCUSSION

In this chapter, we developed a two-dimensional partial differential model based on the laws of continuum mechanics. Like our 1d model in the previous chapter, it also accounts for the three effects that influencing the cell migration, i.e., the driving force of lamellipodia, the motion impeding adhesion between cells and the substrate and the elasticity of the cell layer. To numerically solve the resulting moving-boundary problem, we developed a computation method based the classical finite element method. We should note that the method we choose here works

only for certain geometry (round, ellipse) domain and also we have not calibrated our parameters in the model because of absence of the experimental data.

4.0 AGENT-BASED MODEL OF INFLAMMATION AND WOUND HEALING IN DIABETIC FOOT ULCER

In this chapter, I present a computational model for simulating the behavior of complex system in the wound healing process of Diabetic Foot Ulcer.

4.1 INTRODUCTION

Diabetic foot ulcers (DFU) are caused by both vascular and neurologic complications of diabetes, in combination with persistent opportunistic infections (56,57) and deficient wound healing (58). Over 10 million Americans carry a diagnosis of diabetes, and an estimated 5 million more are undiagnosed diabetics (59). The incidence of foot ulcer in this population approaches 2% per year (60). With reported average treatment costs ranging from $2,500 to almost $14,000 per year, diabetic foot ulcers (DFU) represent a significant financial burden on society (58,60). Additionally, DFU are responsible for more than 50,000 major lower extremity amputations in the United States every year (61). Notably, diabetics with foot ulcers have more than twice the mortality of diabetics with healthy feet (62). Diabetics are known to have elevated levels of TNF (63), and studies have suggested a relatively reduced expression of active TGF-β1 in DFU (64). Both inflammation and wound healing are deranged in chronic, non-healing foot

ulcers, constituting a major complication of diabetes.

Wound healing is a process that involves both inflammation and the resolution of the inflammatory response, which culminates in remodeling (42,43). The first phase of the wound healing response involves the degranulation of platelets and infiltration of inflammatory cells, followed by proliferation of fibroblasts and epithelial cells that deposit collagen and cause contraction of wounds. Rodent models of diabetes display impaired wound repair, with decreased wound tensile strength and collagen deposition in implanted sponges (44). Collagen organization in healing wounds is also poor (44). Furthermore, diabetic wounds have deficits in neovascularization (4) and decreased levels of DNA and protein (44). Pro-inflammatory cytokines such as tumor necrosis factor-α (TNF)(5) and interferon-γ (IFN-γ)(47) inhibit wound healing both *in vitro* and *in vivo.* Interleukin-6 (IL-6), a cytokine central to inflammation (48), is also necessary for proper healing (49). Interleukin-10 (IL-10), a potent anti-inflammatory cytokine, appears to suppress inflammation and induce the remodeling necessary for proper wound healing (50). One cytokine that is central to the wound healing cascade is transforming growth factor-β1 (TGF-β1) (51). TGF-β1, like all isoforms of TGF-β, is produced in a latent form, which must be activated in order to exert its biological effects. The TGF-β1 precursor homodimerizes intracellularly, and is then cleaved extracellularly to yield the active TGF-β1 dimer as well as the remaining portion of its dimerized precursor, the latency-associated peptide (LAP). Under physiological conditions, TGF-β1 is expressed almost completely in its latent form, which consists of the active TGF-β1 dimer bound non-covalently to LAP. Additional proteins such as α2-macroglobulin, latent TGF-β binding proteins, or proteoglycans (e.g. decorin) are bound to latent TGF-β1 in what is known as the large latent complex. Latency-associated peptide and other proteins must be dissociated from latent TGF-β1, in a process

known as activation, before TGF-β1 gains biological activity (52). Of note, there are multiple regulatory intersections among TNF, IL-6, IL-10, IFN-γ, and TGF-β1 (53), and much of this complexity has been captured in our equation-based models of inflammation (54,55).

A standard treatment for DFU is wound debridement, which is effective in approximately 25% of patients (65). In an attempt to improve healing further, numerous studies in animal models of diabetic wound healing have demonstrated efficacy of single growth factors such as platelet-derived growth factor (PDGF) (66), fibroblast growth factor (FGF, acidic or basic) (65), or TGF-β1 (65), these results have often not borne fruit when carried to clinical trials of DFU (67). Though these therapeutic failures suggest that studies should be carried out on DFU patients and tissue/cells derived from these ulcers, we believe that such studies alone are likely insufficient due to the complexity of the wound healing process (68), the complexity of inflammation from which this process stems (53), the co-morbidities (56) and genetic variability in genes such as TGF-β1 (69) in the inflammation/wound healing responses of individual patients.

4.2 MATERIALS AND METHODS

4.2.1 Agent-based Model of Inflammation and Wound Healing

The popularity of ABM lies in the fact that this type of model can simulate the behavior of complex systems in which agents interact with each other and with their environment following local rules based on known physiology. Moreover, the ABM framework accounts for

the stochastic nature of biological processes, in that each rule is a probability of a given event happening; thus, each simulation leads to a unique outcome and can be considered as a separate experiment (or "virtual patient") (79,75). A typical ABM includes three types of elements: region, patch and agent. The region consists of small patches that are uniquely characterized by spatial position, and contain local information. Agents are the objects that can move in the region. The motion of all agents is due to both chemoattraction and stochastic walk, as described in greater detail in the *Appendix B*. We designed an ABM to simulate inflammation and wound healing in a physical domain including skin and underlying soft tissue (the tissue), using *Netlogo* software (Center for Connected Learning and Computer-Based Modeling, Northwestern University, Evanston, IL). First, we created two regions to simulate blood (the source of some of the inflammatory cells that infiltrate injured tissue) and the tissue itself (which contains some inflammatory cells as well as the fibroblasts that will eventually act to heal the injured tissue) (Fig. 4-1). The two regions (blood and tissue) do not intersect: the tissue region is circular and surrounded by the blood region. We used agents to represent the damage (induced by the initial injury as well as by subsequent inflammation, and also a stimulus for further inflammation), as well as resting and activated inflammatory cells (neutrophils, macrophages and fibroblasts). We also used patch variables to represent latent TGF-β1 and the mediators produced by these cells during the inflammation and wound healing stages. The mediators include the pro-inflammatory cytokines

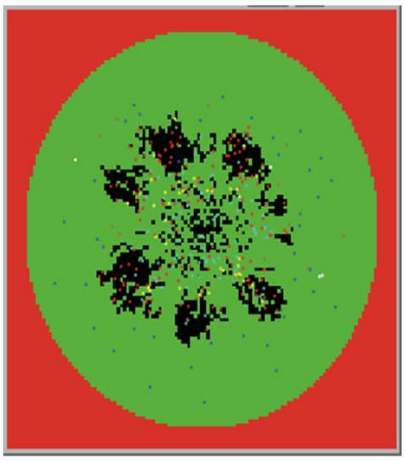

Figure 4-1: The simulation region of Agent Based Model. Red: blood , Blue: tissue.

IL-1β and TNF (both produced by neutrophils and macrophages); the anti-inflammatory cytokines TGF-β1 and IL-10 (both produced by macrophages); and collagen (produced by fibroblasts)(76). Initially, some resting macrophages, neutrophils, fibroblasts and latent TGF-β1 are present with a random distribution both in tissue and blood. By stimulating the tissue with damage in the middle of region, the model creates a chemoattractant gradient (induced by platelet degranulation) (77), which acts to induce the infiltration and activation of both neutrophils and macrophages. Fibroblasts are activated at a later stage both by damage and TGF-β1, to produce collagen that acts to repair both the initial and inflammation-induced damage (77). For a detailed description of rules, please see *Appendix B*.

4.3 RESULTS

4.3.1 Simulating normal tissue healing

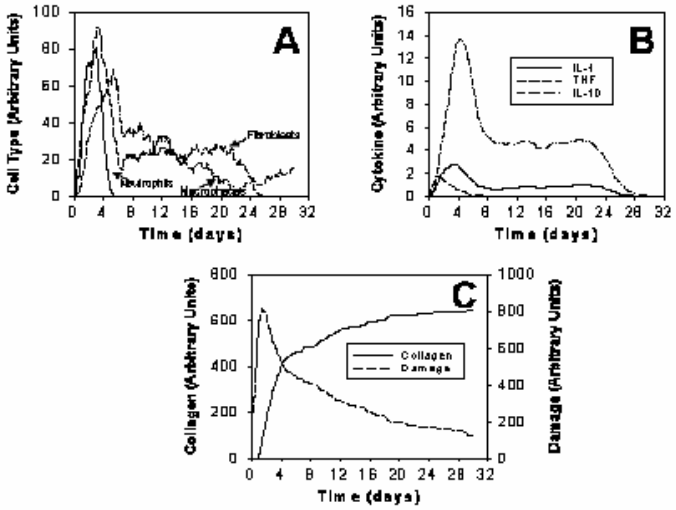

Figure 4-2: **Simulations of baseline wound healing.** Simulations using the ABM were carried out to 30 days, and show the dynamics of inflammatory cells (Panel A), cytokines (Panel B), collagen (Panel C, left y-axis), and tissue damage (Panel C, right y-axis)

Our ABM was capable of reproducing the qualitative features and general time course of skin wound healing, with regards to the dynamics of neutrophils, macrophages, and fibroblasts (Fig. 4-2A); and the inflammatory cytokines IL-1, IL-10, and TNF (Fig. 4-2B). The values in the figures are averaged over the entire space (also in all subsequent figures). Collagen deposition and tissue damage variables served as surrogates for wound healing, and these, too, exhibited the expected qualitative behavior with wound resolution occurring in approximately 1 month (Fig. 4-2C). The simulation presented is one run, representative of the behavior of the ABM under these baseline conditions. In later simulations (see below), we show the variability across simulations at defined time points in the inflammation/healing process. Notably, this simulation did not

address aspects of longer-term collagen remodeling since this aspect of healing was not incorporated in the ABM.

4.3.2 Comparison of normal vs. DFU healing

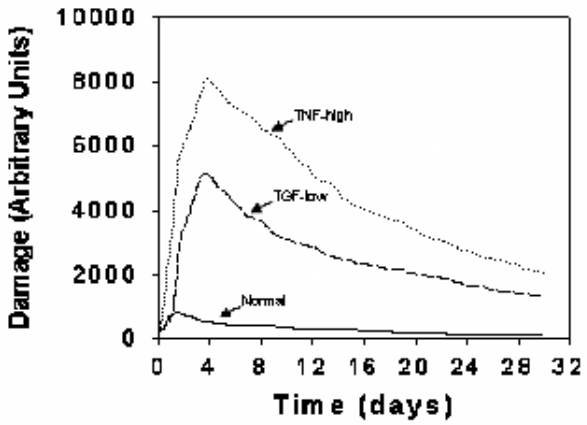

Figure 4-3: **Simulations of healing trajectories in Normal, TNF-high, and TGF-β1-low cases.** The simulated recovery of normal skin tissue damage (i.e., wound healing; solid line) is compared to one of two hypothetical derangements underlying DFU: elevated TNF production (dotted line) or reduced capacity to produce TGF-β1 (dashed line).

We hypothesized that, since inflammation is the initial driver of wound healing, that inflammatory derangements seen in DFU might underlie the delayed healing characteristic of these lesions. Previous studies have suggested that macrophages from diabetics exhibit elevated TNF production (63), and other studies have demonstrated reduced expression of active TGF-β1 (64). TNF and TGF-β1 cross-regulate their own expression and activity in diverse and complex ways, with TNF generally inducing the expression of TGF-β1 and TGF-β1 suppressing the

expression of TNF (78). Accordingly, we hypothesized that either derangement alone might be sufficient to result in altered healing. To test this hypothesis, we simulated the effects of elevated TNF or reduced TGF-β1. In Fig. 4-3, we show the healing trajectories (shown as dynamics of tissue damage) of normal (solid line, reprised from Fig. 4-2C), TNF-high DFU (dotted line), and TGF-β1-low DFU (dashed line). As can be seen, simulated damage in the DFU settings remains elevated as compared to normal wound healing, which we interpret as delayed healing. Thus, as suggested previously (70), the healing trajectories of DFU in these simulations are clearly delayed as compared to normal skin healing. Importantly, this is an emergent property of the system, since the various observations indicative of DFU-like healing have not been programmed into the simulation but rather emerge as a result of changing a single variable (either TNF or TGF-β1).

4.3.3 Simulating clinical variability and known therapies for DFU

We wished to determine if our ABM would result in the sort of patient-to-patient variability that is typically observed clinically with regards to DFU healing. Accordingly, we varied --- and examined our scenarios of normal (Fig. 4-4A), TNF-high (Fig. 4-4B), and TGF-β1-low (Fig. 4-4C) wound healing. These figures show that TNF-high and TGF-β1-low conditions result in higher levels of tissue damage, though our ABM exhibits the type of inter-individual variability previously shown in ABM of acute inflammation (75).

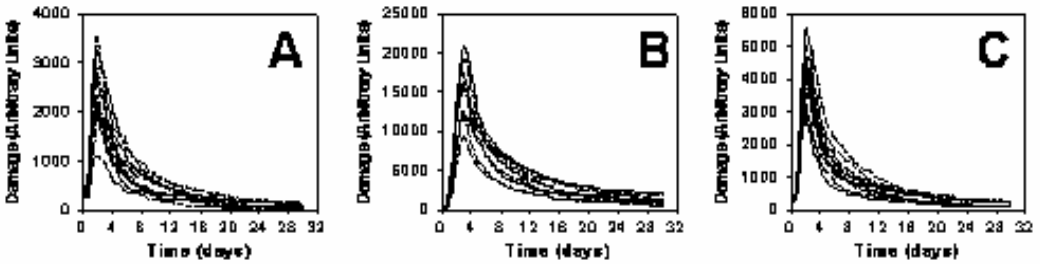

Figure 4-4: **Simulation of the variability in healing trajectories in Normal, TNF-high, and TGF-β1-low cases.** Ten simulations for each case of normal, TNF-high, and TGF-β1-low skin healing were carried out, and the time courses of predicted damage/dysfunction are shown

Debridement, or physical removal of dead or dying tissue, is part of the routine care for DFU, and has been reported to improve healing in ~25% of patients (65). Accordingly, we simulated this procedure by making the assumption that approximately 75% of damaged tissue would be removed at either day 7 or 14 into the time course of healing. Simulated tissue damage was then assessed at day 30. These simulations were carried out in the presence of the inter-individual variability depicted in Figs. 4A-C, in an attempt to determine if the type of variability observed in clinical trials would be seen. Fig. 4-5A demonstrates the elevated damage at simulated day 30 in both TNF-high and TGF-β1-low DFU as compared to normal healing. Interestingly, our simulation suggests that collagen content would be elevated relative to normal healing if DFU were caused by elevated TNF, but the predicted collagen content of DFU derived from low TGF-β1 is predicted to be no different from that of normal controls (Fig. 4-5B). Debridement at day 7 was predicted to result in statistically significant reductions in tissue damage in both TNF-high and TGF-β1-low DFU (Fig. 4-5A). Interestingly, this effect of simulated debridement did not reach statistical significant when simulated debridement was

performed at day 14. In contrast, debridement was not predicted to result in decreased collagen at day 7 or 14, in either TNF-high or TGF-β1-low DFU. These results are in general agreement with clinical studies of debridement (65). We note that in subsequent simulations below, debridement was not simulated in order to be able to gain insight into the single manipulation being studied.

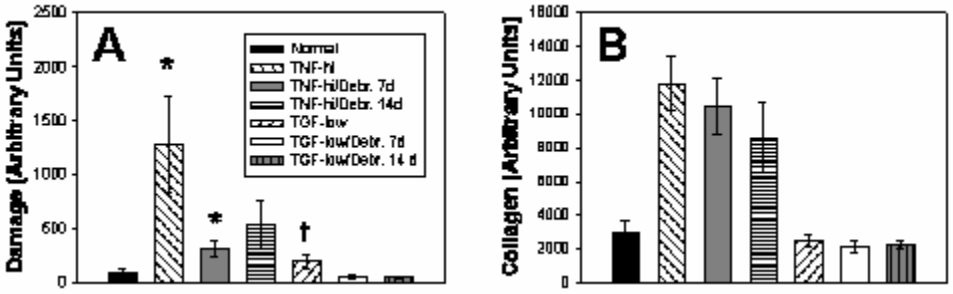

Figure 4-5: **Simulation of debridement of DFU.** Debridement ("Debr.") was simulated as removal of 75% of damaged tissue at the indicated day (either 7 or 14 days post-wounding) in either of two hypothetical derangements underlying DFU: TNF-high or TGF-β1-low (see *Supplementary Materials* for details of normal, TNF-high, and TGF-β1-low simulations.. Simulated tissue damage (Panel A) or collagen content (Panel B) was assessed at day 30 post-wounding. Asterisk: $P < 0.05$ vs. Normal; † = $P < 0.05$ vs. TNF-high.

We also simulated biological therapies for DFU. Although multiple randomized prospective clinical trials have been performed using growth factors in the treatment of DFU, only PDGF has been approved for use (79). PDGF, which is released from platelet granules (80), has been found to increase healing in diabetic neuropathic foot ulcers and is marketed as REGRANEX™ (81). There is also limited evidence to suggest clinical benefit from a platelet releasate that contains many growth factors including PDGF (67,82-84). In order to further validate our ABM, in which platelets are one class of agent, we assessed predicted tissue damage

in the setting of increased platelet-derived factors. We simulated this increase by increasing separately the chemoattractant effect of platelets on macrophages and neutrophils (both effects being parameters in our ABM; see Appendix B). As seen in Fig. 4-6, increasing the chemoattractant effect of platelets on macrophages by 70% and the chemoattractant effect of platelets on neutrophils by 18% resulted in reduced damage under both the increased TNF (dotted line) and reduced TGF-β1 (solid line) cases (compare to the same simulations in Fig. 4-3).

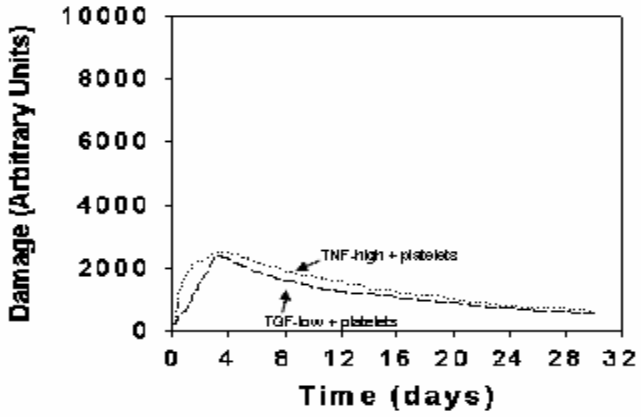

Figure 4-6: **Simulation of PDGF / platelet release therapy for DFU.** The simulation of Fig. 4-3 was repeated, this time in the presence of elevated effects of platelets (increasing the effect of platelets on macrophages by 70% and the effect of platelets on neutrophils by 18%)

This finding arose from a systematic modulation of the relative chemoattracts effects of platelets on macrophages and neutrophils, in a further attempt to explore the potential for our ABM to reproduce inter-patient variability (Tables 4-1 and 4-2). Interestingly, different ratios of the effects of platelets on macrophages and neutrophils were predicted to be either efficacious or non-efficacious at reducing tissue damage in a non-intuitive manner. In the ABM, activated macrophages are assumed to produce TGF-β1, which promotes the healing of DFU and inhibits

TNF production by neutrophils (see the TGF-β1 rule in the *Appendix B*). In turn, activated neutrophils are assumed to produce TNF which not only causes damage but also inhibits TGF-β1 (see the TNF and damage rules in the *Appendix B*). By changing the different potency of activation of macrophages and neutrophils by platelets, the ABM produces different amounts of activated macrophages and activated neutrophils. This change, in turn, leads to the different predicted profiles of TGF-β1, TNF, and damage. Because of these dynamics, either beneficial of detrimental effects of platelets on macrophages and neutrophils are predicted. In all cases, benefit was predicted if the effect of platelets on macrophages was greater than the effect of platelets on neutrophils, and this held true whether we assumed that the underlying cause of DFU was elevated TNF (Table 4-1) or reduced TGF-β1 (Table 4-2). Non-intuitively, if the parameter governing the chemoattractant effect of platelets on neutrophils grew above a certain threshold, the predicted damage was higher than without therapy. We interpret this outcome as signifying that tissue damage mediated by neutrophils exceeds the beneficial effects of the pro-healing elements derived from macrophages. These results may explain why some patients respond to PDGF or platelet releasate and some do not (82,83).

Table 4-1. Simulation of DFU therapy-1. The predicted effect on tissue damage of increasing the chemoattraction of platelets on macrophages (*P1*) and neutrophils (*P2*) was simulated. Macrophages are activated by platelets if the number of platelets is greater than (100 /(1+M*M))/(1+P1), and neutrophils are activated by platelets if the number of platelets is greater than (100/(1+M*1.7)*(M*1.7))/(1+P2). At baseline, P1 = P2 = 0. In this case, DFU were assumed to arise from elevations in TNF production. Healing (assessed at 4-6 days) was assumed to occur if the predicted damage was lower than that predicted for the untreated DFU (8000 arbitrary units; see Fig. 2A, dotted line).

P1 *(% increase over P1 in the TNF-high simulation [Fig. 2a])*	***P2*** *(% increase over P2 in the TNF-high simulation [Fig. 2a])*	***Damage*** *(Arbitrary Units)*	***Healing*** *(relative to no treatment)*
129	19	892	Yes
129	39	5600	Yes
129	≥59	>8000	No
95	19	2000	Yes
95	39	2070	Yes
95	≥59	>8000	No
69	19	2700	Yes
69	≥39	>8000	No
44	19	3100	Yes
44	≥39	>8000	No
34	19	4000	Yes
34	≥39	>8000	No
22	≥19	>8000	No

Table 4-2. Simulation of DFU therapy-2. The predicted effect on tissue damage of increasing the chemoattraction of platelets on macrophages (*P1*) and neutrophils (*P2*) was simulated. Macrophages are activated by platelets if the number of platelets is greater than (100 /(1+M*M))*(1+P1), and neutrophils are activated by platelets if the number of platelets is

(100/(1+M*1.7)*(M*1.7))/(1+P2). At baseline, P1 = P2 = 0. In this case, DFU were assumed to arise from reduced TGF-β1 production. Healing (assessed at 4-6) was assumed to occur if the predicted damage was lower than that predicted for the untreated DFU (3000 arbitrary units; see Fig. 2A, dashed line).

P1 *(% increase over P1 in TGF-β1-low simulation [Fig. 2a])*	***P2*** *(% increase over P2 in the TGF-β1-low simulation [Fig. 2a])*	***Damage*** *(Arbitrary Units)*	***Healing*** *(relative to no treatment)*
170	19	1400	Yes
150	19	1600	Yes
129	19	2000	Yes
129	>39	>3000	No
95	≥19	>3000	No
69	19	2700	~Equal
69	≥39	>3000	No
44	19	2300	Yes
44	≥39	>3000	No
34	19	3500	No
34	≥39	>3000	No
22	≥19	>3000	No

4.3.4 Inflammatory and Healing Characteristics of simulated DFU

Having demonstrated that the overall qualitative simulations are valid, we next wished to examine the characteristics associated with healing in simulations of normal tissue and the two ways of simulating DFU (TNF-high and TGF-β1-low). These simulations were all examined at 2.5 days in order to examine early drivers of the inflammatory and healing responses. In all cases, we carried out ten simulations of each condition, since the ABM platform is inherently stochastic (85). This approach allowed us to simulate several "patients" and also to carry out a statistical analysis (Kruskall-Wallis ANOVA on ranks followed by Tukey post-hoc test) to ascertain group differences (considered significant at $P < 0.05$). As seen in Fig. 4-7, the qualitative features of simulated wound healing either in the setting of elevated TNF production (gray bars) or reduced TGF-β1 production (hatched bars) as compared to normal healing (black bars) are largely similar: elevated neutrophil influx (Fig. 4-7A), elevated TNF expression (Fig. 4-7B), elevated IL-10 (Fig. 4-7C), reduced collagen deposition (Fig. 4-7E), and increased tissue damage (Fig. 4-7F). In general, these are all hallmarks of DFU. Interestingly, decreased TGF-β1 expression as compared to normal healing was observed in the simulations in which DFU were presumed to arise from reduced TGF-β1 (as expected, Fig. 4-7D, hatched bar), but this was not the case in simulations in which TNF was over-produced (Fig. 4-7D, gray bar).

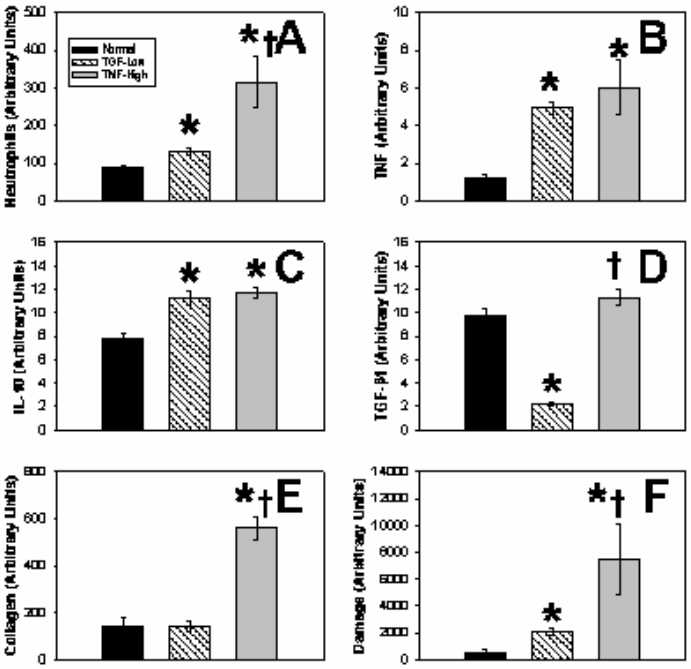

Figure 4-7: **Simulations of inflammation and healing parameters in normal, TNF-high, and TGF-β1-low cases.** The simulated levels of neutrophils (Panel A), TNF (Panel B), IL-10 (Panel C), TGF-β1 (Panel D), collagen (Panel E), and tissue damage (Panel F) are shown for normal skin healing (black bars) and two hypothetical derangements underlying DFU: elevated TNF production (gray bars) or reduced capacity to produce TGF-β1 (hatched bars). *: $P < 0.05$ vs. Normal; †: $P < 0.05$ vs. TGF-β1-low (all by Kruskall-Wallis ANOVA on ranks followed by Tukey post-hoc test).

4.3.5 Simulating hypothetical therapies for DFU

We next sought to simulate therapies for DFU. Numerous studies in animal models of diabetic wound healing have demonstrated the efficacy of topical administration of single growth factors such as PDGF (66), acidic or basic FGF (44), or TGF-β1 (44). However, these results have not been confirmed in clinical trials of DFU (79). In an attempt to determine if *in silico* methodologies could suggest some insights into therapy design for DFU, we applied simulated

therapeutic strategies to our simulations of delayed healing depicted in Fig. 4-7. Since both elevated TNF and reduced TGF-β1 gave generally similar qualitative patterns of inflammatory and healing derangements, we tested the simulated therapies under settings of either elevated TNF (Fig. 4-8) or reduced TGF-β1 (Fig. 4-9). The therapies we chose to simulate are directly related to these derangements: neutralizing antibodies to TNF (anti-TNF), agents that increase the rate of TGF-β1 activation, and latent TGF-β1 itself. The rationale for these interventions was the following. In the case of anti-TNF, FDA-approved anti-TNF antibodies are available for the treatment of several inflammatory diseases, with further indications likely (86); additionally, we have carried out previous work on simulating mathematically the actions of anti-TNF in the setting of sepsis (87). TGF-β1 modulation (either provision of TGF-β1 or its inhibition) has been proposed as a possible therapy for various aspects of aberrant wound healing (88). TGF-β1, like all other isoforms of TGF-β, is synthesized in a biologically inactive (latent) state and must be activated through various mechanisms in order to bind to its cognate receptor complex and exert its diverse biological functions (52). Treatment with active TGF-β1 as well as TGF-β2 has been attempted in the setting of DFU, with initially promising results but ultimately lack of statistically significant efficacy (54,55). One reason for this lack of overall efficacy might be that active TGF-β1 has a shorter half-life than latent TGF-β1 (52). In the case of TGF-β1 activation, As seen in Figs. 4-8 and 4-9, we carried out ten simulations of each condition, and assessed statistical significance by Kruskall-Wallis ANOVA on ranks followed by Tukey post-hoc test.

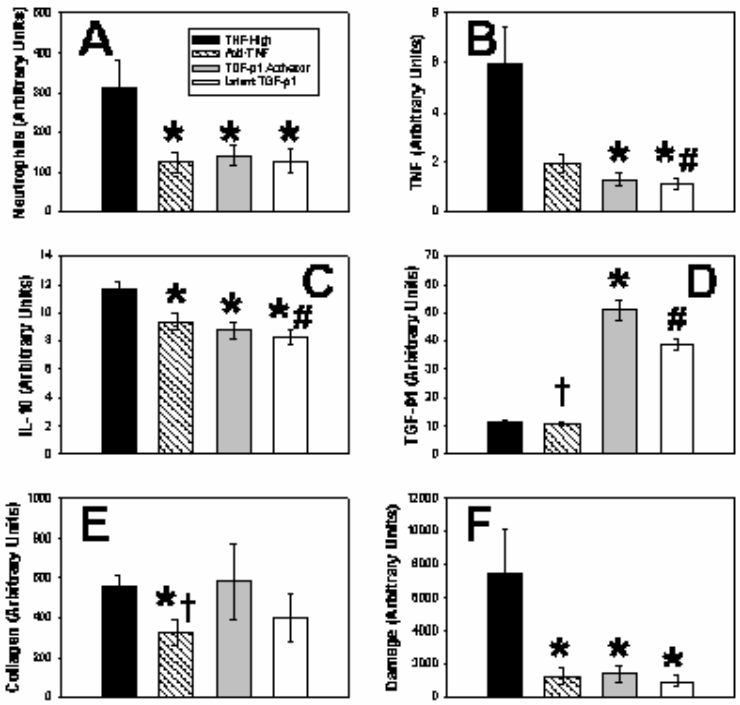

Figure 4-8: **Simulations of therapies in TNF-high DFU.** The simulated levels of neutrophils (Panel A), TNF (Panel B), IL-10 (Panel C), TGF-β1 (Panel D), collagen (Panel E), and tissue damage (Panel F) are shown for skin healing in DFU assumed to arise due to elevated TNF production (black bars). Also simulated are three hypothetical therapies: anti-TNF neutralizing antibodies (hatched bars), an agent that activates endogenous latent TGF-β1 (gray bars), and treatment with latent TGF-β1 (open bars). *: P< 0.05 vs. TNF-high baseline; †: P< 0.05 vs. TGF-β1 activator; #: P< 0.05 vs. anti-TNF (all by Kruskall-Wallis ANOVA on ranks followed by Tukey post-hoc test)

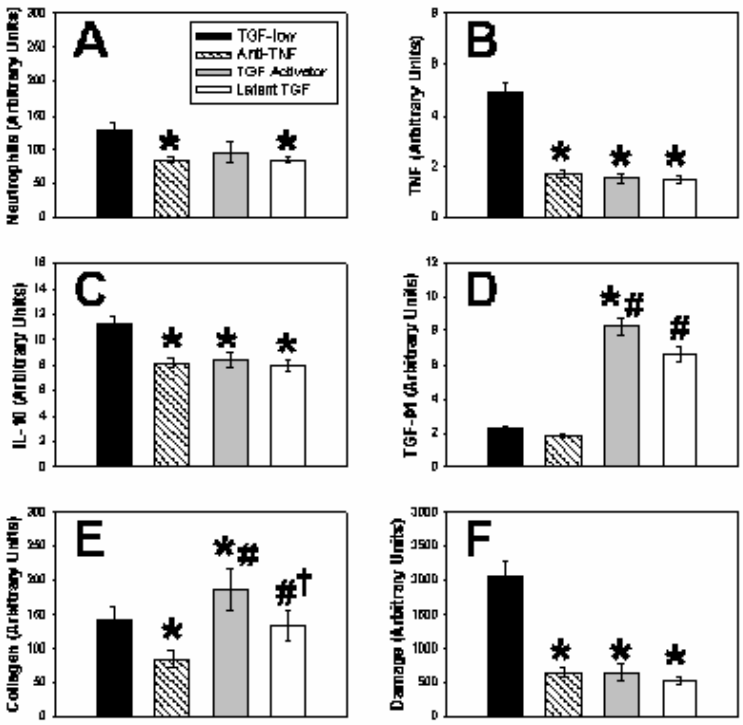

Figure 4-9: **Simulations of therapies in TGF-β1-low DFU.** The simulated levels of neutrophils (Panel A), TNF (Panel B), IL-10 (Panel C), TGF-β1 (Panel D), collagen (Panel E), and tissue damage (Panel F) are shown for skin healing in DFU assumed to arise due to reduced TGF-β1 production (black bars). Also simulated are three hypothetical therapies: anti-TNF neutralizing antibodies (hatched bars), an agent that activates endogenous latent TGF-β1 (gray bars), and treatment with latent TGF-β1 (open bars). *: $P< 0.05$ vs. TGF-β1-low baseline; †: $P< 0.05$ vs. TGF-β1 activator; #: $P< 0.05$ vs. anti-TNF (all by Kruskall-Wallis ANOVA on ranks followed by Tukey post-hoc test).

Regardless of whether DFU healing was simulated as stemming from elevated TNF production (Fig. 4-8) or reduced TGF-β1 production (Fig. 4-9), all three therapies (anti-TNF [hatched bars], latent TGF-β1 [open bars], or TGF-β1 activation [gray bars]) were predicted to suppress neutrophil influx (Figs. 4-8A and 4-9A) and tissue damage (Figs. 4-8F and 4-9F) to the same, statistically significant degree as compared to the DFU baseline (black bars). Interestingly,

our simulations suggested that all three therapies would result in a reduction of TNF production in DFU tissue (Fig. 4-8B and 4-9B), though the effect of anti-TNF would not be statistically significant if the cause of DFU was elevated TNF production. Our simulation suggested that provision of latent TGF-β1 or activation of endogenous TGF-β1 would elevate overall TGF-β1 expression regardless of the presumed cause (high TNF or low TGF-β1) of DFU pathology (Figs. 4-8D and 4-9D). Interestingly, only the TGF-β1 activator was predicted to increase collagen deposition in a statistically significant fashion, and only upon assumption of reduced baseline TGF-β1 as a cause of DFU. Another non-intuitive finding was the suggestion that anti-TNF would decrease collagen levels above those of baseline DFU (Figs. 4-8E and 4-9E), while at the same time reducing overall tissue damage (Figs. 4-8F and 4-9F).

4.4 DISCUSSION

Chronic wounds are a serious health care problem, costing billions of dollars each year and carry unaccounted but considerable suffering and anguish. DFU, in particular, are a major cause of amputation (58,60). There has been great interest in treating DFU with growth factors in recent years. One might suggest that use of growth factors to heal a DFU would result in improved healing and a lowered amputation rate (79). Unfortunately, the number of amputations performed in the United States each year remains essentially unchanged (58,60).

In order to attempt to break the logjam of compounds available for clinical trials in the setting of DFU, we created an ABM simulation of the inflammation/wound healing process. Our

specific objectives were 1) to use this ABM to test hypotheses regarding the genesis of DFU and 2) to test *in silico* possible therapies for DFU. In the process of validating our ABM, we were able to simulate existing therapies for DFU (debridement and platelet releasate / PDGF).

The literature regarding the inflammatory genesis of DFU is sparse. However, two possible mechanisms stand out: elevated TNF (63) and reduced TGF-β1 (64). Since both of these cytokines are highly interrelated in their biology, we incorporated several of these interactions in our model. Our simulations suggest that for many indices of inflammation and healing, the effects of elevated TNF and reduced TGF-β1 are very similar. Due to the interrelationships between TNF and TGF-β1, both elevated TNF and reduced TGF-β1 are predicted to be associated with increased inflammatory infiltrates, elevated TNF and IL-10, reduced collagen, and elevated tissue damage. However, only the simulation in which TGF-β1 is reduced, and not the case in which TNF is elevated, is predicted to be associated with the reported decreased expression of TGF-β1 in DFU (44). Thus, our simulations support the hypothesis that a central derangement in skin healing that leads to DFU is the reduced expression of TGF-β1. Nonetheless, it is possible or perhaps even likely that more than one cause of DFU exists. Given the overall qualitative similarity between the features of healing in the setting of reduced TGF-β1 and elevated TNF, both mechanisms (and others as well) may be operant in DFU. Further clinical studies are needed in order to address this issue. In any case, these different assumptions can be used in the *in silico* design and testing of DFU therapeutics, since this variability could be used to create simulated clinical trials; we (44,87) and others (75) have demonstrated the utility of this approach in the setting of sepsis.

Whether elevated TNF or reduced TGF-β1 underlies the pathology of DFU, our ABM is capable of reproducing the effect of known therapies for DFU. A major type of intervention is

debridement, in which necrotic and/or infected areas of a DFU are removed surgically. Studies have shown that debridement improves healing in ~25% of patients (65). When we simulated the removal of 75% of damaged tissue at either 7 or 14 d from the onset of a wound, our ABM suggested that this would result in a statistically significant reduction in tissue damage at 30 d without a change in collagen levels, interpreted by us to mean improved healing. It might be argued that our finding of reduced tissue damage upon simulated removal of damaged tissue would seem obvious, but the finding that collagen levels remain the same suggests that indeed our ABM is depicting healing.

Although multiple randomized prospective clinical trials have been performed using growth factors in the treatment of DFU, only one growth factor, PDGF, has been approved for use (79). PDGF has been found to increase healing in diabetic neuropathic foot ulcers and is marketed as REGRANEX™ (81). There is only limited evidence to suggest clinical benefit from other growth factors, including TGF-β1, FGF, IGF-1, GM-CSF, EGF, or a platelet releasate that contains many growth factors (79,82,83,94-101). In our simulation, we account for the effects of platelet releasate and PDGF through the inclusion of platelets which function to chemoattract macrophages and neutrophils (see Tables 4-1 and 4-2 as well as the *Appendix B*). Though we do not simulate PDGF explicitly, we demonstrate that modulating the actions platelets on macrophages and neutrophils can, under certain circumstances, result in reduced tissue damage as compared to that predicted to be found in untreated DFU. Moreover, our exploration of the relative effects of platelets on macrophages and neutrophils suggested that there would be great variability in the efficacy of platelet-related therapies (either PDGF or platelet releasate). Thus, these simulations may be of benefit when attempting to personalize this type of therapy to an

individual patient, if *ex vivo* studies could be carried out to assess the chemoattractant effect of the therapeutic agent on a patient-by-patient basis.

This interaction between inflammation and wound healing in the setting of DFU therapy may also be seen in other ways. In the clinical trials of PDGF, the importance of debridement became apparent. The first clinical trial to demonstrate benefit from PDGF found that extensive debridement, that is, wound excision down to normal tissue beyond the wound space, was associated with the highest healing rate (65). "Wound excision" was favored, as this procedure removed the tissue with the highest bacterial load and the highest concentration of proteases. It may also be that the tissues removed were those trapped in the inflammatory phase of healing, with elevated TNF and reduced TGF-β1, a clinical observation that supports the findings of our simulations.

We utilized an *in silico* approach to study several hypothetical therapeutic approaches. The first agent we examined was a neutralizing anti-TNF antibody, given that elevated TNF production is a feature of diabetes (43) and given our ability to simulate many of the characteristics of DFU by assuming elevated TNF production. Several FDA-approved anti-TNF antibodies are available for the treatment of various inflammatory diseases (86). Our findings also suggest that anti-TNF therapy for DFU should be explored.

Another therapy that we simulated was one in which exogenous, latent TGF-β1 would be provided or one that would lead to the activation of endogenous TGF-β1. TGF-β1 modulation (either provision of TGF-β1 or its inhibition) has been proposed as a possible therapy for various aspects of aberrant wound healing (88). However, treatment with TGF-β1 was not efficacious as a DFU therapeutic (89). We reasoned that since latent TGF-β1 has a longer half-life than active TGF-β1 (52), it might serve as a better therapeutic agent. Our findings support this hypothesis.

The main disadvantage of our model is that it is based on the key mechanisms of inflammation and wound healing, but like any simulation does not incorporate all possible biological mechanisms that might be operant in the process of inflammation and wound healing. Importantly, our ABM does not account for collagen contraction as part of the wound healing process, though it is our aim to incorporate this mechanism in later iterations of the model. It should be noted that in the ABM framework, it is often difficult to define the direct or indirect role of a given variable in the final outcome, and so the more mechanistic rules an ABM contains the less likely we are to gain this type of insight. Moreover, the more complex the ABM, the greater the computing power necessary to run any single simulation. In this manuscript, we strove to balance model realism with tractability, and believe that the overall findings justify this compromise. Also, the agent-based model structure contains certain assumptions regarding the stochastic nature of some of the processes being modeled, and these assumptions may not represent the exact way in which these processes occur *in vivo*. Another limitation relates to the way in which one models the production and clearance of a given agent, as well as the exact effects than an agent has on another agent: we have tried to base our assumptions on literature data whenever possible, but the literature is incomplete with regards to certain specific interactions. Finally, this ABM is calibrated with regards to literature data on skin wound healing, but has not been specifically calibrated or validated with prospective data from DFU patients, a deficiency we are currently in the process of addressing.

APPENDIX A

We present the numerical method used to solve Eq. 9. Let $0 = s^1 < s^2 < \cdots < s^N = 1$ be a subdivision of (0,1), such that $s^{j+1} - s^j = 1/N = \Delta s$, the mesh size. Let $\Delta t > 0$ be a given step size and let $t^i = i\Delta t$. Let x_i^j denote the numerical approximation of $x(t^i, s^j)$ Equation 9 is rewritten as:

$$\frac{\partial x}{\partial t} = \kappa\left(\frac{(\partial^2 x/\partial s^2)}{(\partial x/\partial s)^2} - \frac{\rho'(s)t}{\partial x/\partial s}\right). \qquad \text{(A.1)}$$

Using the finite difference approximations of the partial derivatives of *x*, we obtain the following combined implicit/explicit scheme that is second order in space and first order in time (note that explicit difference has been used in the denominator and implicit difference in the numerator):

$$\frac{x_{i+1}^j - x_i^j}{\Delta t} = \kappa\left(\frac{4(x_{i+1}^{j+1} - 2x_{i+1}^j + x_{i+1}^{j-1})}{(x_i^{j+1} - x_i^{j-1})^2} - \frac{2\Delta s\rho'(s^j)t^{i+1}}{x_i^{j+1} - x_i^{j-1}}\right), \qquad i \geq 0, \quad 2 \leq j \leq N-1 \quad \text{(A.2)}$$

After rearranging the terms, we obtain:

$$M_i^j x_{i+1}^{j+1} - (2M_i^j + 1)x_{i+1}^j + M_i^j x_{i+1}^{j-1} = -x_i^j + u_j^i, \quad i \geq 0, \quad 2 \leq j \leq N-1 \qquad \text{(A.3)}$$

with M_i^j and u_i^j are as defined below:

$$M_i^j = \frac{4\kappa\Delta t}{(x_i^{j+1} - x_i^{j-1})^2}$$
$$u_i^j = \frac{2\kappa\Delta t\Delta s\rho'(s^j)t^{i+1}}{x_i^{j+1} - x_i^{j-1}} \tag{A.4}$$

The initial condition is simply $x_0^j = s^j$ and the boundary conditions yield:

$$x_i^1 = 0, \quad x_i^N = x_i^{N-1} + \Delta s e^{\phi+\rho(1)t^i}, \quad i \geq 0 \tag{A.5}$$

The solution x_{i+1}^j at the time step $i + 1$ can be found by solving the linear system

$$A\begin{pmatrix} x_{i+1}^2 \\ x_{i+1}^3 \\ \vdots \\ x_{i+1}^{N-2} \\ x_{i+1}^{N-1} \end{pmatrix} = \begin{pmatrix} -x_i^2 + u_i^2 \\ -x_i^3 + u_i^3 \\ \vdots \\ -x_i^{N-2} + +u_i^{N-2} \\ -x_i^{N-1} + u_i^{N-1} - M_i^{N-1}\left[\Delta s e^{\phi+\rho(1)t^{i+1}}\right] \end{pmatrix} \tag{A.6}$$

where

$$A = \begin{pmatrix} -(2M_i^2+1) & M_i^2 & 0 & \cdots & 0 \\ M_i^3 & -(2M_i^3+1) & M_i^3 & \cdots & 0 \\ \vdots & \vdots & \ddots & \cdots & \vdots \\ 0 & \cdots & M_i^{N-2} & -(2M_i^{N-2}+1) & M_i^{N-2} \\ 0 & \cdots & 0 & M_i^{N-1} & -(2M_i^{N-1}+1)+M_i^{N-1} \end{pmatrix} \tag{A.7}$$

APPENDIX B

ABM Rules

World. The "world" is a square grid, 120 x 120 patches, with origin in the center of the grid. X and Y coordinates thus take values in the range of -60 to 60. The tissue region is a circle of diameter 55 centered at the origin.

Time scale. We assumed in the model that 1 unit of simulated time represents 0.069 day, or about 1.6 hours. The time resolution of the simulation is in the millisecond range, thus much smaller than a time unit. This assumption results in complete healing (defined as return of the damage variable to baseline) in the normal scenario by ~30 days. All of the dynamics of cells and cytokines are therefore appropriately scaled to give realistic time courses.

Lifespans and Half-lives. The lifespan was assumed to be 1-3 days for neutrophils, 4-6 days for macrophages and 5-7 days for fibroblasts. Cytokine half-lives were assumed to be 2-3 days. We note the half life of latent TGF- β1 is much larger than the half life of activated TGF-β1 (102). Activated fibroblasts proliferate every three days.

Initialization. We arbitrarily set the total number of resting neutrophils and macrophages to 80 each, and the number of resting fibroblasts was set to 30. The location and age of these cells was randomly distributed in both blood and tissue. The initial total amount of damage was set to M*M, where M is a number set by the user. In our simulations, we set M = 16. This damage was randomly distributed inside the disk centered at the origin of the domain and with

diameter equal to M. The initial number of platelets p(x,y) was spatially distributed according to the formula (100/(1+x^2+y^2)), where (x,y) are grid coordinates. This type of distribution for the platelets is crucial for the initialization of the inflammatory process. The initial values of IL-1β, TNF, activated TGF-β1, IL-10, and collagen were set to zero. The initial amount of latent TGF-β1 was set to 10.

Activation. In this simulation, neutrophils and macrophage are chemoattracted by platelets (76) as well as TNF (76) while fibroblasts are chemoattracted by TGF-β1 (76). In actuality, platelets release several growth factors in addition to TGF-β1, such as PDGF, transforming growth factors α (TGF-α), epidermal growth factor (EGF), and insulin-like growth factor –I (IGF-I) to activate macrophages and neutrophils (76). However, in our model we do not include all of these growth factors, but rather assume, for simplicity, that platelets can activate those inflammatory cells in the following way: Macrophages are activated by platelets if the number of platelets is greater than (100 /(1+M*M))/(1+P1), where M represents the magnitude of the damage, and are activated by TNF if TNF > 0.1 and P1 represents the potency of chemoattraction by platelets. At baseline, P1 = P2 = 0. Neutrophils are activated by platelets if the number of platelets is greater than (100/(1+M*1.7)*(M*1.7))/(1+P2), where M represents the magnitude of the damage, and are activated by TNF if TNF > 0.2. P2 represents the potency of chemoattraction of neutrophils by platelets. At baseline, P1 = P2 = 0. For the studies depicted in Tables 1 and 2, only the activation portion (not the random walk; see below) is modulated. Fibroblasts are activated by TGF-β1 if TGF-β1>0.2 and damage is present.

Cell motion: chemoattraction and stochastic motion

The motion of all agents is due to both chemoattraction and random walk. First, neutrophils and macrophage are chemoattracted by platelets (76) as well as TNF (76) while fibroblasts are chemoattracted by TGF-β1 (76). Second, every unit time, the direction of cells is randomly changed. The final motion is a direct superposition of the random walk and chemoattractant-directed motion. For the studies depicted in Tables 4-1 and 4-2, only the chemoattractant portion (not the random walk) is modulated.

Mediators

1. TNF:

1. Produced by activated macrophages and activated neutrophils. Inhibited by TGF-β1 and IL-10 and elevated by TNF and IL1-β (77). In the TNF-overproducing simulation, for activated macrophages, the dynamics of TNF are calculated by the equation: TNF = TNF + 0.044 * (1 / (0.1 + TGF * 100 + IL-10 / 100)) * (1 + TNF + IL1-beta / 10))). For activated neutrophils, the dynamics of TNF are calculated by the equation: TNF = TNF + 2.2* (1 / (0.1 + TGF * 100 + IL-10 / 100)) * (1 + TNF + IL1-beta / 10))). In the simulation of TNF-overproducing with anti-TNF antibody treatment, for activated macrophages, these dynamics are calculated by the equation: TNF = TNF + 0.0293 * (1 / (0. 1 + TGF * 100 + IL-10 / 100)) * (1 + TNF + IL1-beta / 10))). For activated neutrophils, these dynamics are calculated by the equation: TNF = TNF + 1.467* (1 / (0.1 + TGF * 100 + IL-10 / 100)) * (1 + TNF + IL1-beta / 10))). In the simulation of TGF-β1-under-production with anti-TNF antibody treatment, for activated macrophages, these dynamics are calculated by the equation: TNF = TNF + 0.0067 * (1 / (0. 1 + TGF * 100 + IL-10 / 100)) * (1 + TNF + IL1-beta /

10))). For activated neutrophils, these dynamics are calculated by the equation: TNF = TNF + 0.33* (1 / (0.1 + TGF * 100 + IL-10 / 100)) * (1 + TNF + IL1-beta / 10))). In the other simulations, for activated macrophages, these dynamics are calculated by the equation: TNF = TNF + 0.02 * (1 / (0.1 + TGF * 100 + IL-10 / 100)) * (1 + TNF + IL1-beta / 10))). For activated neutrophils, these dynamics are calculated by the equation: TNF = TNF + (1 / (0.1 + TGF * 100 + IL-10 / 100)) * (1 + TNF + IL1-beta / 10))).

2. Biological function: Inhibit the expression of TGF-β1 and IL-10 in activated macrophages. Stimulate the expression of TNF and IL-1β in activated macrophages and neutrophils. Activate latent TGF-β1, macrophages, and neutrophils (77).
3. TNF diffuses in the following sense: periodically (every 0.1 unit time) each patch shares 100 percent of the value of the patch with its 8 neighboring patches.

2. TGF-β1:

1. Activated from latent-TGF-β1 by TNF and IL1-β: if TNF>0.2 or IL1-β > 0.2, then TGF =TGF + latent-TGF * 0.001; latent-TGF=latent-TGF * 0.999. In the simulations of latent-TGF treatment, the initial value of latent-TGF equals four. In the other simulations, the initial value of latent-TGF equals one.
2. Produced by activated macrophages and activated fibroblasts. Inhibited by TNF (77). In the simulations of TGF-β1-under-production, for activated macrophages, TGF-β1 dynamics are calculated by the equation: TGF=TGF + latent-TGF * 0.03 / (1 + TNF*10). For activated fibroblasts, these dynamics are calculated by the equation: TGF=TGF + 0.015 / (1 + TNF/5). In the simulations of TGF-β1-under-production with TGF-β1 activation treatment, for activated macrophages, TGF-β1 dynamics are calculated by the equation: TGF=TGF + latent-TGF *0.15/ (1 + TNF*10). For activated fibroblasts, these dynamics are calculated by

the equation: TGF=TGF + 0.075 / (1 + TNF/5). In the simulations of TNF-overproducing with TGF-β1 activation treatment, for activated macrophages, TGF-β1 dynamics are calculated by the equation: TGF=TGF + latent-TGF / (1 + TNF*10). For activated fibroblasts, these dynamics are calculated by the equation: TGF=TGF + 0.5 / (1 + TNF/5). In the other simulations, for activated macrophages, these dynamics are calculated by the equation: TGF=TGF + latent-TGF * 0.2 / (1 + TNF*10). For activated neutrophils, these dynamics are calculated by the equation: TGF=TGF + 0.1 / (1 + TNF/5).

3. Biological function: Inhibit expression of TNF and IL-1β in activated macrophages and neutrophils; chemoattract and activate fibroblasts (77).
4. TGF-β1 diffuses in the following sense: periodically (every 0.1 s) each patch shares 100 percent of the value of the patch with its 8 neighboring patches.

3. IL-1β:

1. Produced by activated macrophage and neutrophils. Inhibited by TGF-β1 and IL-10 (78). Elevated by TNF and IL1-β. The dynamics of IL-1β are calculated by the equation: IL1-beta=IL1-beta + 0.2 / (1 + TGF*2+IL-10/100)*(1+TNF+IL1-beta).
2. Biological function: Simulate TNF and IL-1β expression in activated macrophages and neutrophils. Increase TGF-β1 activation (52,76,77).
3. IL-1β diffuses in the following sense: periodically (every 0.1 s) each patch shares 100 percent of the value of the patch with its 8 neighboring patches

4.IL-10:

1. Produced by activated macrophages. The dynamics of IL-10 are calculated by the equation: IL1-10=IL1-10+1.

2. Biological function: Inhibit TNF (78,103) and IL-1β (78) expression in activated macrophages and neutrophils.
3. IL-10 diffuses in the following sense: periodically (every 0.1 unit time) each patch shares 100 percent of the value of the patch with its 8 neighboring patches.

5. Collagen:

1. Produced by activated fibroblasts. Inhibited by TNF and elevated by TGF-β1 (46). In our model, we also required that the amount of collagen produced not exceed the existing amount of damage in the same patch. Collagen dynamics are calculated by the equation: (if damage > 2 * total-TGF / (1 + total-TNF), collagen=collagen + 2 * total-TGF / (1 + total-TNF)) else collagen=collagen + damage).

2. Biological function: tissue repair (76,77).

Source Terms

In the simulation, there are damage-dependent sources for resting macrophages and resting neutrophils randomly distributed in the tissue and blood. The number of newly created neutrophils is a function of the total amount A of damage: 2*(A/1500+1) every 0.5 time units until 2.7 days of simulated time are reached. The number of newly created macrophage is a function of the total amount A of damage: A/15000+1 every 2 time units until 20 days of simulated time are reached. There is also a constant source (two cells per every four time units) for resting fibroblasts randomly distributed in the tissue and blood if damage exists.

Damage: In addition to initial damage, damage can also be created by TNF if TNF > 0.25. Damage is healed by collagen (if collagen>0. damage=damage –1.collagen=collagen -1), and it also has 0.2% chance for self-healing every time unit.

REFERENCE

1. Feng, J., El-Assal, O. N., and Besner, G. E. Heparin-binding EGF-like growth factor (HB-EGF) and necrotizing enterocolitis. Semin. Pediatr. Surg. 2005;14:167-174.

2. Warner, B. W., and Warner, B. B. Role of epidermal growth factor in the pathogenesis of neonatal necrotizing enterocolitis. Semin. Pediatr. Surg. 2005;14:175-180.

3. Henry, M. C., and Moss, R. L. Surgical therapy for necrotizing enterocolitis: Bringing evidence to the bedside. Semin. Pediatr. Surg. 2005;14:181-190.

4. Hsueh, W., Caplan, M. S., Qu, X. W., Tan, X. D., De Plaen, I. G., and Gonzales-Crussi, F. Neonatal necrotizing enterocolitis: clinical considerations and pathogenetic concepts. Pediatr. Dev. Pathol.2003; 6:6-23.

5. Cetin, S., Dunkelberger, J., Li, J., Boyle, P., Qureshi, F., Ford, H. R., Upperman, J. S., Watkins, S., and Hackam, D. J. Endotoxin differentially modulates the basolateral and apical sodium/proton exchangers (NHE) in enterocytes. *Surgery.* in press.

6. Waller, D., Thomas, N., and Self, T. Epithelial restitution in the large intestine of the rat following insult with bile salts. *Virchows. Arch. A Pathol. Anat. Histopathol.* 1988; 414:77-81.

7. Mammen, J., and Matthews, J. Mucosal repair in the gastrointestinal tract. *Crit. Care Med*. 2003; 31:S532-S537.

8 Cetin, S., Ford, H.R., Sysko, L.R., Agarwal, C., Wang, J., Neal, M.D., Baty, C., Apodaca, G., and Hackam, D.J. Endotoxin inhibits intestinal epithelial restitution through activation of Rho-GTPase and increased focal adhesions. *J Biol Chem.* 2004;279:24592-600.9.

9. Qureshi, F. G., Leaphart, C., Cetin, S., Li., J., Grishin, S., Watkins, S., Ford, H. R., and Hackam, D. J. Increased expression and function of integrins in enterocytes by endotoxin impairs epithelial restitution. *Gastroenterology* 2005;128:1012-1022.

10. Palecek, S.P., Loftus, J. C., Ginsberg, M.H., Lauffenburger, D.A, and Horwitz, A.F. Integrin-ligand binding properties govern cell migration speed through cell-substratum adhesiveness. *Nature* 1997;385:537-540.

11. Holly S. P., Larson, M. K., and Parise, L. V. Multiple roles of integrins in cell motility. *Exp. Cell. Res*. 2000;261:69-74.

12. Sherratt, J.A., and Murray, J. D. Models of epidermal wound healing. *Proc. Biol. Sci.* 1990;241:29-36.

13. Sherratt, J.A. Actin aggregation and embryonic epidermal wound healing. *J. Math. Biol.* 1993;31:703-716.

14. Murray, J.D., and Oster, G.F. Generation of biological pattern and form. *IMA J. Math. Appl. Med. Biol.* 1994;1:51-75.

15. Walker, D.C., Hill, G., Wood, S.M., Smallwood, R.H., and Southgate, J. Agent-based computational modeling of epithelial cell monolayers: predicting the effect of exogenous calcium concentration on the rate of wound closure. *IEEE Trans. NanoBioscience.* 2004;3:153-163.

16. Walker, D.C., Southgate, J., Hill, G., Holcombe, M.,Hose, D.R., Wood, S.M., MacNeil, S., and Smallwood, R.H. The epihome:modeling the social behaviour of cells, *Biosystems.* 2004;76:89-100.

17. Tranquillo, R.T., and Murray, J.D., Mechanistic model of wound contraction. *J. Surg. Res.* 1993;55:233-247.

18. Olsen, L., Sherratt, J.A., and Maini, P.K. A mechanochemical model for adult dermal wound contraction and the permanence of the contracted tissue displacement profile. *J. Theor. Biol.* 1995;177:113-128.

19. Dallon, J.C., Sherratt, J.A., and Maini, P.K. Modeling the effects of transforming growth factor β on extracellular matrix alignment in dermal wound repair. *Wound Repair Regen.* 2001;9:278-286.

20. DiMilla, P.A., Barbee, K., and Lauffenburger, D.A. Mathematical model for the effects of adhesion and mechanics on cell migration speed. *Biophys. J.* 1991;60:15-37.

21. Mi, Q., Rivière, B., Clermont, G., Steed, D. L., and Vodovotz, Y. Agent-based model of inflammation and wound healing: insights into diabetic foot ulcer pathology and the role of transforming growth factor-b1. *Wound Repair Regen.* 2007 In press.

22. Sheetz, M.P., Felsenfeld, D.P, and Galbraith, C.G. Cell migration: regulation of force on extracellular matrix-integrin complexes. *Trends Cell Biol.* 1998 8:51-54.

23. Anand, R.J., Leaphart, C.L., Mollen, K.P., and Hackam, D.J. The role of the intestinal barrier in the pathogenesis of necrotizing enterocolitis. *Shock.* 2007;27:124-133.

24. Fung, Y. C. *Biomechanics: Mechanical Properties of Living Tissues*. Springer 1993, New York.

25. Canetta, E., Duperray, A., Leyrat, A., Verdier, C. Measuring cell viscoelastic properties using a force-spectrometer: Influence of protein-cytoplasm interactions. *Biorheology*. 2005;42:321-333.

26. Maini, P.K., McElwain, S. and Leavesley, D. Traveling waves in a wound healing assay. *Applied Math. Lett.* 2004;17:575-580.

27. Prass, M. Jacobson, K., Mogilner, A., and Radmacher, M. Direct measurement of the lamellipodial protrusive force in a migrating cell. *J. Cell. Biol.* 2006;174:767-772.

28. Leaphart, C.L., Qureshi, F., Cetin, S., Li, J., Dubowski, T., Batey, C., Beer-Stolz, D., Guo, F., Murray, S.A., and Hackam, D.J. Interferon-gamma Inhibits Intestinal Restitution by Preventing Gap Junction Communication Between Enterocytes. *Gastroenterology.* 2007*;* 132:2395-2411.

29. Cetin, S., Leaphart, C.L., Li, J., Ischenko, I., Hayman, M., Upperman, J., Zamora, R., Watkins, S., Ford, H.R., Wang, J., Hackam, D.J. Nitric oxide inhibits enterocyte migration through activation of RhoA-GTPase in a SHP-2-dependent manner. *Am J Physiol Gastrointest Liver Physiol*. 2007;292:G1347-58.

30. J. S. Upperman, B. Lugo, V. Camerini, I. Yotov, J. Rubin, G. Clermont, R. Zamora, G. B. Ermentrout, H. R. Ford, and Y. Vodovotz. Mathematical modeling in NEC - A new look at an ongoing problem. *J.Pediatr.Surg.* 2007;42:445-453,

31. Vodovotz, Y. Deciphering the complexity of acute inflammation using mathematical models. *Immunologic Res.* 2006;36:237-246

32. Brewitt, H. Sliding of epithelium in experimental corneal wounds. A scanning electron microscopic study *Acta Ophthalmol.(Copenh)* 1979;57 (6):945-958

33. Matsuda, M., Sawa,M., Edelhauser, H.F. Bartels,S.P., Neufeld, A.H. and Kenyon, K.R. Cellular migration and morphology in corneal endothelial wound repair. 1985. *Invest Ophthalmol.Vis.Sci* 1985;26 (4):443-449

34. Ballestrem, C., Hinz, B., Imhof, B.A. and Wehrle-Haller, B. Marching at the front and dragging behind: differential alphaVbeta3-integrin turnover regulates focal adhesion behavior. *J Cell Biol.* 2001;155 (7):1319-1332

35. Mi, Q., Swigon., D., Rivière, B., Cetin, Selma., Vodovotz, Y and Hackam D. One-dimensional Elastic Continuum Model of Enterocyte Layer Migration. *Biophys. J.* 2007 In press.

36. McElwain, D. and Pettet, G. Cell migration in multicell spheroids: swimming against the tide, *Bull. Math. Biol.* 1993*;*55,655-674.

37. Xinfu Chen, Shangbin Cui and Avner Friedman, A Hyperbolic free boundary problem modeling tumor growth:asymptotic behavior. *Transactions of the A.M.S,* 2005;Volume 357, Number 12, Pages 4771-4804

38. Crank, J. Free and moving boundary problems. Clarendon Press 1984

39. Reddy, J. N. An Introduction to the Finite Element Method. McGraw-Hill Book Co., New York, 1984, 1993, 2005

40. Hall, C., Porsching, T. Numerical Analysis of partial differential equations. Prentice-Hall, Inc 1990

41. Persson,P.O., Strang, G. A Simple Mesh Generator in MATLAB. *SIAM Review,* 2004;Volume 46 (2), pp. 329-345

42. . Hart J. Inflammation. 1: Its role in the healing of acute wounds. *J Wound Care* 2002;11(6):205-9.

43. Hart J. Inflammation. 2: Its role in the healing of chronic wounds. *J Wound Care* 2002;11(7):245-9.

44. Broadley KN, Aquino AM, Hicks B, Ditesheim JA, McGee GS, Demetriou AA, Woodward SC, Davidson JM. Growth factors bFGF and TGF beta accelerate the rate of wound repair in normal and in diabetic rats. *Int J Tissue React* 1988;10(6):345-53.

45. Fahey TJ, III, Sadaty A, Jones WG, Barber A, Smoller B, Shires GT. Diabetes impairs the late inflammatory response to wound healing. *J Surg Res* 1991;50(4):308-13.

46. Rapala K. The effect of tumor necrosis factor-alpha on wound healing. An experimental study. *Ann Chir Gynaecol Suppl* 1996;211:1-53.

47. Adelmann-Grill BC, Hein R, Wach F, Krieg T. Inhibition of fibroblast chemotaxis by recombinant human interferon gamma and interferon alpha. *J Cell Physiol* 1987; 130(2):270-5.

48. Kamimura D, Ishihara K, Hirano T. IL-6 signal transduction and its physiological roles: the signal orchestration model. *Rev Physiol Biochem Pharmacol* 2003;149:1-38.

49. Gallucci RM, Simeonova PP, Matheson JM, Kommineni C, Guriel JL, Sugawara T, Luster MI. Impaired cutaneous wound healing in interleukin-6-deficient and immunosuppressed mice. *FASEB J* 2000;14(15):2525-31.

50. Ohshima T, Sato Y. Time-dependent expression of interleukin-10 (IL-10) mRNA during the early phase of skin wound healing as a possible indicator of wound vitality. *Int J Legal Med* 1998;111(5):251-5.

51. Roberts AB, Sporn MB. Transforming growth factor-β. In: Clark RAF, editor. The Molecular and Cellular Biology of Wound Repair. New York: Plenum Press, 1996:275-308.

52. Annes JP, Munger JS, Rifkin DB. Making sense of latent TGFbeta activation. *J Cell Sci* 2003;116(Pt 2):217-24.

53. Nathan C. Points of control in inflammation. *Nature* 2002;420(6917):846-52.

54. Vodovotz Y, Clermont G, Chow C, An G. Mathematical models of the acute inflammatory response. *Curr Opin Crit Care* 2004;10:383-90.

55. Chow CC, Clermont G, Kumar R, Lagoa C, Tawadrous Z, Gallo D, Betten B, Bartels J, Constantine G, Fink MP, Billiar TR, Vodovotz Y. The acute inflammatory response in diverse shock states. *Shock* 2005;24:74-84.

56. Boulton AJ, Meneses P, Ennis WJ. Diabetic foot ulcers: A framework for prevention and care. *Wound Repair Regen* 1999;7(1):7-16.

57. Browne AC, Sibbald RG. The diabetic neuropathic ulcer: an overview. *Ostomy Wound Manage* 1999;45(1A Suppl):6S-20S.

58. Morain WD, Colen LB. Wound healing in diabetes mellitus. Clin Plast Surg 1990;17(3):493-501.

59. Harris MI, Flegal KM, Cowie CC, Eberhardt MS, Goldstein DE, Little RR, Wiedmeyer HM, Byrd-Holt DD. Prevalence of diabetes, impaired fasting glucose, and impaired glucose tolerance in U.S. adults. *The Third National Health and Nutrition Examination Survey*, 1988-1994. Diabetes Care 1998;21(4):518-24.

60. Ramsey SD, Newton K, Blough D, McCulloch DK, Sandhu N, Reiber GE, Wagner EH. Incidence, outcomes, and cost of foot ulcers in patients with diabetes. *Diabetes Care* 1999;22(3):382-7.

61. Levin ME. Diabetic foot ulcers: pathogenesis and management. *J et Nurs* 1993(5):191-8.

62. Boyko EJ, Ahroni JH, Smith DG, Davignon D. Increased mortality associated with diabetic foot ulcer. *Diabet Med* 1996;13(11):967-72.

63. Hussain MJ, Peakman M, Gallati H, Lo SS, Hawa M, Viberti GC, Watkins PJ, Leslie RD, Vergani D. Elevated serum levels of macrophage-derived cytokines precede and accompany the onset of IDDM. *Diabetologia* 1996;39(1):60-9.

64. Jude EB, Blakytny R, Bulmer J, Boulton AJ, Ferguson MW. Transforming growth factor beta 1, 2, 3 and receptor type I and II in diabetic foot ulcers. *Diabet Med* 2002;19(6):440-7.

65. Steed DL, Donohoe D, Webster MW, Lindsley L. Effect of extensive debridement and treatment on the healing of diabetic foot ulcers. Diabetic Ulcer Study Group. *J Am Coll Surg* 1996;183(1):61-4.

66. Greenhalgh DG, Sprugel KH, Murray MJ, Ross R. PDGF and FGF stimulate wound healing in the genetically diabetic mouse. *Am J Pathol* 1990;136(6):1235-46.

67. Steed DL. Modifying the wound healing response with exogenous growth factors. *Clin Plast Surg* 1998;25(3):397-405.

68. Sherratt JA, Dallon JC. Theoretical models of wound healing: past successes and future challenges. *C R Biol* 2002;325(5):557-64.

69. Bayat A, Bock O, Mrowietz U, Ollier WE, Ferguson MW. Genetic susceptibility to keloid disease and hypertrophic scarring: transforming growth factor beta1 common polymorphisms and plasma levels. *Plast Reconstr Surg* 2003;111(2):535-43.

70. Steed DL. Wound-healing trajectories. *Surg Clin North Am* 2003;83(3):547-vii.

71. Murray JD, Maini PK, Tranquillo R. Mechanochemical models for generating biological pattern and form in development. Physics Rep 1988;171:59-84.

72. Murray JD. Mathematical Biology. Heidelberg (Germany): Springer-Verlag, 1989.

73. Tranquillo RT, Murray JD. Continuum model of fibroblast-driven wound contraction: inflammation-mediation. J Theor Biol 1992;158(2):135-72.

74. Cook, J. A mathematical model for dermal wound healing: wound contraction and scar formation. 1995. University of Washington (Seattle). Ref Type: Thesis/Dissertation

75. An G. In-silico experiments of existing and hypothetical cytokine-directed clinical trials using agent based modeling. *Crit Care Med* 2004;32:2050-60.

76. Cockbill S. Wounds: The healing process. *Hosp Pharmacist* 2002;9:255-60.

77. Witte MB, Barbul A. General principles of wound healing. *Surg Clin North Am* 1997;77(3):509-28.

78. Letterio JJ, Vodovotz Y, Bogdan C. TGF-β and IL-10: Inhibitory Cytokines Regulating Immunity and the Response to Infection. In: Henderson B, Higgs G, editors. Novel Cytokine Inhibitors. Basel: *Birkhauser Verlag*, 2000:217-42.

79. Richard JL, Parer-Richard C, Daures JP, Clouet S, Vannereau D, Bringer J, Rodier M, Jacob C, Comte-Bardonnet M. Effect of topical basic fibroblast growth factor on the healing of chronic diabetic neuropathic ulcer of the foot. A pilot, randomized, double-blind, placebo-controlled study. *Diabetes Care* 1995;18(1):64-9.

80. Heldin CH, Westermark B. Mechanism of action and in vivo role of platelet-derived growth factor. *Physiol Rev* 1999;79(4):1283-316.

81 Robson MC, Payne WG, Garner WL, Biundo J, Giacalone V, Cooper D, Ouyang P. Integrating the results of Phase IV (postmarketing) clinical trial with four previous trials reinforces the position that Regranex (becaplemin) gel 0.01% is an effective adjunct to the treatment of diabetic foot ulcers. *J Appl Res* 2005;**5**:35-45.

82. Steed DL, Goslen JB, Holloway GA, Malone JM, Bunt TJ, Webster MW. Randomized prospective double-blind trial in healing chronic diabetic foot ulcers. CT-102 activated platelet supernatant, topical versus placebo. *Diabetes Care* 1992;15(11):1598-604.

83. Holloway G, Steed D, DeMarco M, Matsumoto T, Moosa H, Webster M. A randomized, controlled multicenter, dose response trial of activated platelet supernatant, topical CT-102 in chronic, non-healing, diabetic wounds. *WOUNDS* 1993;**5**:198-206.

84. Moulin V, Lawny F, Barritault D, Caruelle JP. Platelet releasate treatment improves skin healing in diabetic rats through endogenous growth factor secretion. *Cell Mol Biol* (Noisy -le-grand) 1998;44(6):961-71.

85.. Ermentrout GB, Edelstein-Keshet L. Cellular automata approaches to biological modeling. *J Theor Biol* 1993;160(1):97-133.

86. Calamia KT. Current and future use of anti-TNF agents in the treatment of autoimmune, inflammatory disorders. *Adv Exp Med Biol* 2003;528:545-9.

87 Clermont G, Bartels J, Kumar R, Constantine G, Vodovotz Y, Chow C. *In silico* design of clinical trials: a method coming of age. *Crit Care Med* 2004;32:2061-70.

88. Carter K. Growth factors: the wound healing therapy of the future. *Br J Community Nurs* 2003;8(9):S15-9, S22.

89. Robson MC, Steed DL, Franz MG. Wound healing: biologic features and approaches to maximize healing trajectories. *Curr Probl Surg* 2001;38(2):72-140.

90. Bennett SP, Griffiths GD, Schor AM, Leese GP, Schor SL. Growth factors in the treatment of diabetic foot ulcers. *Br J Surg* 2003;90(2):133-46.

91. Vodovotz Y, Chesler L, Chong H, Kim SJ, Simpson JT, DeGraff W, Cox GW, Roberts AB, Wink DA, Barcellos-Hoff MH. Regulation of transforming growth factor-β1 by nitric oxide. *Cancer Res* 1999;59:2142-9.

92. Luckhart S, Crampton AL, Zamora R, Lieber MJ, Dos Santos PC, Peterson TML, Emmith N, Lim J, Wink DA, Vodovotz Y. Mammalian transforming growth factor-β1 activated after ingestion by *Anopheles stephensi* modulates mosquito immunity. *Infect Immun* 2003;71:3000-9.

93. Schwentker A, Vodovotz Y, Weller R, Billiar TR. Nitric oxide and wound repair: role of cytokines? *Nitric Oxide* 2002;7:1-10.

94. Mulder GD, Patt LM, Sanders L, Altman M, Hanley M, Duncan G. Enhanced healing of ulcers in patients with diabetes by topical treatment with glycyl-l –histidy-l-lysine. *Wound Rep Reg* 1994;2:256-69.

95. Atri SC, Misra J, Bisht D, Misra K. Use of homologous platelet factors in achieving total healing of recalcitrant skin ulcers. *Surgery* 1990;108(3):508-12.

96. Knighton DR, Ciresi KF, Fiegel VD, Austin LL, Butler EL. Classification and treatment of chronic nonhealing wounds. Successful treatment with autologous platelet-derived wound healing factors (PDWHF). *Ann Surg* 1986;204(3):322-30.

97. Robson MC, Steed DL, McPherson JM, Prett BM. Effects of transforming growth factors β2 on wound healing in diabetic foot ulcers. *J Appl Res* 2002;**2**:133-45.

98. Agrawal RP, Agrawal S, Beniwal S, Joshi CP, Kochar DK. Granulocyte-macrophage colony-stimulating factor in foot ulcers. *Diabetic Foot* 2003;**6**:93-7.

99. de Lalla F, Pellizzer G, Strazzabosco M, Martini Z, Du JG, Lora L, Fabris P, Benedetti P, Erle G. Randomized prospective controlled trial of recombinant granulocyte colony-stimulating factor as adjunctive therapy for limb-threatening diabetic foot infection. *Antimicrob Agents Chemother* 2001;45(4):1094-8.

100. Gough A, Clapperton M, Rolando N, Foster AV, Philpott-Howard J, Edmonds ME. Randomised placebo-controlled trial of granulocyte-colony stimulating factor in diabetic foot infection. *Lancet* 1997;350(9081):855-9.

101. Tsang MW, Wong WK, Hung CS, Lai KM, Tang W, Cheung EY, Kam G, Leung L, Chan CW, Chu CM, Lam EK. Human epidermal growth factor enhances healing of diabetic foot ulcers. *Diabetes Care* 2003;26(6):1856-61.

102. O'Connor-McCourt MD, Wakefield LM. Latent transforming growth factor-β in serum: A specific complex with α2-macroglobulin. *J Biol Chem* 1987;262:14090-9.

103. Bogdan C, Vodovotz Y, Nathan CF. Macrophage deactivation by interleukin 10. *J Exp Med* 1991;174:1549-55.